

Review

# Pure and Yb-Doped $\text{La}_x\text{Y}_y\text{Sc}_{4-x-y}(\text{BO}_3)_4$ Crystals: A Review of Recent Advances

Alin Broasca <sup>1,2</sup>, Madalin Greculeasa <sup>1,2</sup>, Flavius Voicu <sup>1</sup>, Cristina Gheorghe <sup>1</sup> and Lucian Gheorghe <sup>1,\*</sup><sup>1</sup> National Institute for Laser, Plasma and Radiation Physics, 077125 Magurele, Romania<sup>2</sup> Doctoral School of Physics, Faculty of Physics, University of Bucharest, 077125 Magurele, Romania

\* Correspondence: lucian.gheorghe@inflpr.ro

**Abstract:** This paper reviews the progress in developing the  $\text{La}_x\text{Y}_y\text{Sc}_{4-x-y}(\text{BO}_3)_4$ -LYSB and Yb-doped  $\text{La}_x\text{Y}_y\text{Sc}_{4-x-y}(\text{BO}_3)_4$ -LYSB:Yb huntite-type crystals grown by the Czochralski method as new candidates for the next generation of nonlinear optical (NLO) and/or laser crystals. Considering the incongruent melting of these crystals, the initial compositions of the melt and the pulling and rotation rates were optimized. Additionally, a special thermal setup was engineered to grow LYSB-type crystals by the Czochralski crystal growth method. The chemical compositions of the LYSB and LYSB:Yb grown crystals were found to be  $\text{La}_{0.78}\text{Y}_{0.32}\text{Sc}_{2.90}(\text{BO}_3)_4$  and  $\text{La}_{0.78}\text{Y}_{0.32}\text{Yb}_{0.04}\text{Sc}_{2.86}(\text{BO}_3)_4$ , respectively. Therefore, for the LYSB:Yb crystal, the doping concentration of  $\text{Yb}^{3+}$  ions was considered to be 4 at.% with respect to the nonstoichiometric  $(\text{La}_{1-x}\text{Y}_x)_{1.25}\text{Sc}_{2.75}(\text{BO}_3)_4$  undoped compounds, i.e., LYSB:Yb (4 at.%). In terms of NLO properties, the obtained results demonstrate that LYSB and LYSB:Yb (4 at.%) crystals possess remarkable properties specific to huntite-type crystals. The main advantage of these crystals consists in the fact that they may be obtained with large dimensions and excellent optical quality by the Czochralski method, which recommends them as a new class of highly efficient crystals for different NLO applications, including second harmonic generation (SHG) of high-power or high-energy laser beams. The laser performances of the LYSB:Yb (4 at.%) crystal prove its favorable intrinsic properties to generate laser emissions in the 1  $\mu\text{m}$  range with high efficiency. The efficient laser emission at  $\sim 1028$  nm together with good NLO characteristics to convert its own emission into emission at  $\sim 514$  nm via SHG make the LYSB:Yb (4 at.%) crystal a very promising active medium to be used in self-frequency doubling configuration.



**Citation:** Broasca, A.; Greculeasa, M.; Voicu, F.; Gheorghe, C.; Gheorghe, L. Pure and Yb-Doped  $\text{La}_x\text{Y}_y\text{Sc}_{4-x-y}(\text{BO}_3)_4$  Crystals: A Review of Recent Advances. *Crystals* **2023**, *13*, 169. <https://doi.org/10.3390/cryst13020169>

Academic Editor: Guanying Chen

Received: 19 December 2022

Revised: 15 January 2023

Accepted: 16 January 2023

Published: 18 January 2023



**Copyright:** © 2023 by the authors. Licensee MDPI, Basel, Switzerland. This article is an open access article distributed under the terms and conditions of the Creative Commons Attribution (CC BY) license (<https://creativecommons.org/licenses/by/4.0/>).

**Keywords:** single crystals; Czochralski; NLO crystals;  $\text{Yb}^{3+}$ ; laser crystals

## 1. Introduction

Nonlinear optical (NLO) crystals play a key role in the emergence of optoelectronic and photonic technologies, as they have the ability to change the characteristics of a laser beam in terms of frequency, amplitude, phase, and polarization. In the context of expanding laser applications over a wide variety of domains, the pursuit of new NLO crystals has attracted more interest in the scientific community. The specific criteria that a NLO crystal should meet are the following: (i) crystallizing in noncentrosymmetric structure ( $\chi^{(2)} \neq 0$ ); (ii) high transparency in the spectral range of interest; (iii) large nonlinear optical coefficients; (iv) moderate birefringence to meet the phase-matching conditions, especially in the UV spectral range; (v) large laser-induced damage threshold (LDT); (vi) chemical stability and good physical properties; and, last but not least, (vii) the possibility of obtaining crystals with large dimensions and high quality. Since the 1980s, more than a hundred different NLO crystals have been developed and studied. Among these, NLO crystals from the borate family, such as  $\beta$ - $\text{BaB}_2\text{O}_4$  ( $\beta$ -BBO),  $\text{LiB}_3\text{O}_5$  (LBO),  $\text{CsLiB}_6\text{O}_{10}$  (CLBO),  $\text{GdCa}_4\text{O}(\text{BO}_3)_3$  (GdCOB),  $\text{YCa}_4\text{O}(\text{BO}_3)_3$  (YCOB), and  $\text{YAl}_3(\text{BO}_3)_4$  (YAB), stood out for their good NLO properties. However, the main disadvantage of BBO, LBO, CLBO, and YAB crystals is that they have incongruent melting and can be obtained only by the flux

crystal growth method, which involves complex and long-time growth processes as well as some limitations in the grown crystal dimension and quality. Two types of borate crystal are known to melt congruently or include congruently melting compounds that can be grown with large size and high quality by the Czochralski method: (i) rare-earth calcium oxyborates RCOB (R = Gd, Y, La) and (ii) binary borates  $\text{LnMe}_3(\text{BO}_3)_4$  (Ln = lanthanide, Me = Al, Ga, Sc) with trigonal huntite-type structure [1]. On the basis of the anionic group theory [2], huntite-type borates are predicted to possess very good NLO properties as a result of their favorable structure containing parallel-aligned  $(\text{BO}_3)^{3-}$  anionic groups. The most recognized member of this family is YAB crystal, because it presents the highest nonlinear efficiency ( $d_{11@1064\text{nm}} = 1.5 \pm 0.1 \text{ pm V}^{-1}$ ) and also the highest laser damage threshold (0.4–0.6 GW/cm<sup>2</sup>) [3,4], but, as pointed out, it has the disadvantage of incongruent melting. In order to overcome the limitations imposed by the growth technology, research has focused on the development of huntite-type compounds based on scandium (Sc) cations  $\text{LnSc}_3(\text{BO}_3)_4$  that can crystallize in various structural phases depending on the ratio of the ionic radius of Ln and the ionic radius of Sc ( $r_{\text{Ln}}/r_{\text{Sc}}$ ) [5]. For instance,  $\text{LaSc}_3(\text{BO}_3)_4$ -LSB (Ln = La) crystallize in the monoclinic system with space group  $C2/c$  (centrosymmetric), whereas  $\text{YSc}_3(\text{BO}_3)_4$ -YSB (Ln = Y) crystallize in the trigonal system with space group  $R32$  (noncentrosymmetric) isostructural with huntite mineral  $\text{CaMg}_3(\text{CO}_3)_4$ . Given that in centrosymmetric crystals the nonlinear susceptibility of second order ( $\chi^{(2)}$ ) is zero, research focused on changing the LSB structure from monoclinic to trigonal structure by doping with Ln ions having smaller ionic radii, e.g.,  $\text{La}_{1-x}\text{Nd}_x\text{Sc}_3(\text{BO}_3)_4$  or  $\text{La}_x\text{Y}_y\text{Sc}_{4-x-y}(\text{BO}_3)_4$ ,  $\text{La}_x\text{Lu}_y\text{Sc}_{4-x-y}(\text{BO}_3)_4$ ,  $\text{Bi}_x\text{La}_y\text{Sc}_{4-x-y}(\text{BO}_3)_4$ , and  $\text{La}_x\text{Gd}_y\text{Sc}_{4-x-y}(\text{BO}_3)_4$  [6–11]. Even though these compounds have incongruent melting, it was proved that, with the appropriate composition and a suitable thermal setup, the  $\text{La}_x\text{Y}_y\text{Sc}_{4-x-y}(\text{BO}_3)_4$ -LYSB and  $\text{La}_x\text{Gd}_y\text{Sc}_{4-x-y}(\text{BO}_3)_4$ -LGSB crystals could be grown by the Czochralski crystal growth technique [12,13]. This paper reviews the progress of developing the LYSB and Yb-doped  $\text{La}_x\text{Y}_y\text{Sc}_{4-x-y}(\text{BO}_3)_4$ -LYSB:Yb crystals obtained by the Czochralski method as new candidates for the next generation of NLO and/or laser crystals.

## 2. Huntite-Type $\text{La}_x\text{Y}_y\text{Sc}_{4-x-y}(\text{BO}_3)_4$ Crystal

### 2.1. Material Synthesis and Czochralski Growth

In a first approximation, based on the fact that the difference between the ionic radii of  $\text{La}^{3+}$  and  $\text{Y}^{3+}$  ions is smaller than that of  $\text{Y}^{3+}$  and  $\text{Sc}^{3+}$  ions in six-fold coordination ( $r_{\text{La}}-r_{\text{Y}} = 0.132 \text{ \AA}$  and  $r_{\text{Y}}-r_{\text{Sc}} = 0.155 \text{ \AA}$ ) [14], in order to determine the minimum doping concentration with Y cations in the LSB structure that leads to the trigonal phase formation as the majority phase, we assumed that  $\text{Y}^{3+}$  ions replaced only  $\text{La}^{3+}$  cations in the LSB structure. This meant that, in this approximation, the general formula of LYSB was presumed to be  $\text{La}_{1-x}\text{Y}_x\text{Sc}_3(\text{BO}_3)_4$ . Therefore, different  $\text{La}_{1-x}\text{Y}_x\text{Sc}_3(\text{BO}_3)_4$  compounds with  $0 \leq x \leq 0.6$  were synthesized by the solid-state reaction method. Oxide powders of 5N purity ( $\text{La}_2\text{O}_3$ ,  $\text{Y}_2\text{O}_3$ , and  $\text{Sc}_2\text{O}_3$ ) and 99.98%  $\text{B}_2\text{O}_3$  were used as starting materials. Considering the evaporation of  $\text{B}_2\text{O}_3$  during the synthesis of polycrystalline compounds, to the stoichiometric amounts was added an excess of  $\text{B}_2\text{O}_3$  (5 wt. %). Before weighing, the oxide powders of  $\text{Sc}_2\text{O}_3$ ,  $\text{Y}_2\text{O}_3$ , and  $\text{La}_2\text{O}_3$  were heated for 12 h at 1000 °C in air to eliminate absorbed water. Then, the powders were mixed, pressed into tablets, and sintered in atmospheric air for 24 h at 1300 °C. The X-ray powder diffraction (XRPD) spectra were measured at room temperature in the  $2\theta$  range of 10°–60° using a PANalytical Empyrean X-ray diffractometer ( $\lambda = 1.5406 \text{ \AA}$ ). XRPD spectra of the polycrystalline compounds  $\text{La}_{1-x}\text{Y}_x\text{Sc}_3(\text{BO}_3)_4$  having x from 0 at. % to 60 at. % are presented in Figure 1. As can be seen, the phase transition from the monoclinic structure of LSB (space group  $C2/c$ ) to the trigonal structure of LYSB (space group  $R32$ ) was achieved for a Y concentration over 40 at. %. However, there were still some diffraction peaks that were not indexed by the trigonal structure. Therefore, the Rietveld method was employed to quantify each phase of the compounds with  $x > 40$  at. %. As expected, the analysis revealed the existence of one dominant trigonal phase (space group  $R32$ ) in a proportion larger than 93 wt. % and two minority phases, the monoclinic

phase (space  $C2/c$ ) and the cubic phase of  $Sc_2O_3$ , which were quantified to be smaller than 2 wt. % and 5 wt. %, respectively, in all synthesized compounds.

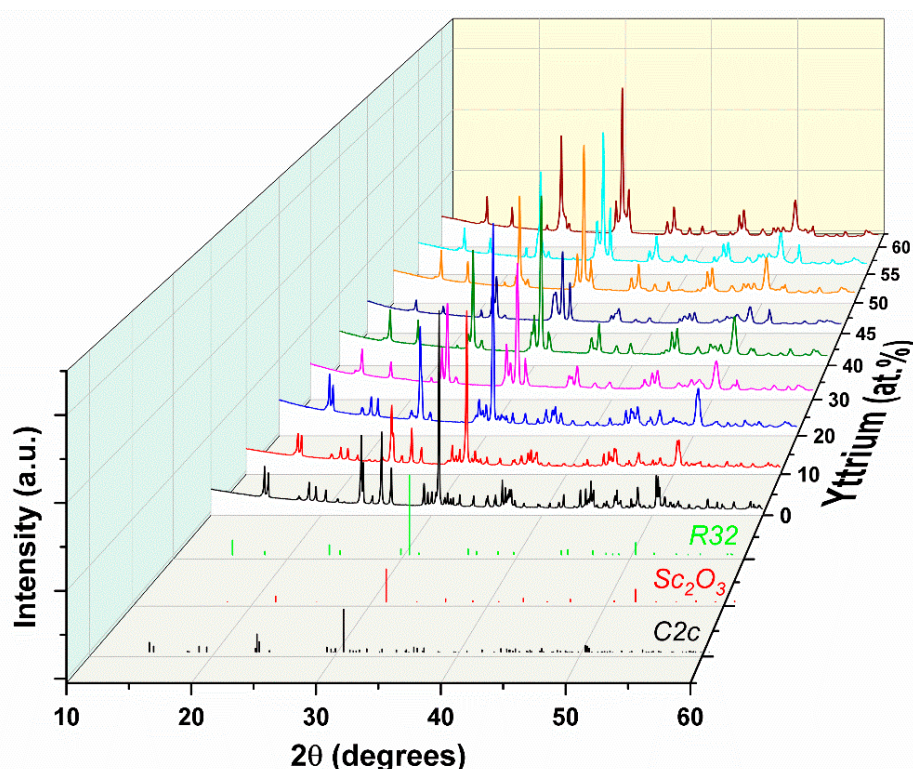


**Figure 1.** Room-temperature XRPD spectra of  $La_{1-x}Y_xSc_3(BO_3)_4$  polycrystalline compounds. The vertical bars in black, red, and green are associated with PDF card 01-087-1665 of  $C2/c$  monoclinic phase, PDF card 04-001-2439 of cubic  $Sc_2O_3$  phase, and PDF card 04-018-1225 of  $R32$  trigonal phase, respectively. (Adapted with permission from ref. [13], copyright 2019 American Chemical Society).

To test the second harmonic generation (SHG) property of the  $La_{1-x}Y_xSc_3(BO_3)_4$  compounds having  $x > 0.4$ , a Q-smart 850 Nd:YAG laser with emission at 1064 nm (10 Hz, 6 ns) was employed. All of the investigated compounds generated green light, thus confirming that they had  $\chi^{(2)} \neq 0$ .

Knowing the compositional domain regarding the achieving of the phase transition to the trigonal structure, we proceeded to the growth of the LYSB crystal by the Czochralski method. It is well known that  $La_xY_ySc_z(BO_3)_4$  ( $x + y + z = 4$ ) are peritectic compounds and that, in order to crystallize the trigonal phase, a deficiency of  $ScBO_3$ , i.e.,  $z < 3$ , or a surplus of  $LaBO_3$ - $YBO_3$  is required in the initial melt [5]. Considering this,  $La_{0.754}Y_{0.546}Sc_{2.70}(BO_3)_4$ ,  $La_{0.765}Y_{0.485}Sc_{2.75}(BO_3)_4$ ,  $La_{0.7875}Y_{0.4625}Sc_{2.75}(BO_3)_4$ ,  $La_{0.8625}Y_{0.4375}Sc_{2.70}(BO_3)_4$ , and  $La_{0.8125}Y_{0.4375}Sc_{2.75}(BO_3)_4$  nonstoichiometric compounds were synthesized by the solid-state reaction method using the same procedure described above and used as starting compounds (initial melt compositions) to grow, by the Czochralski technique, LYSB-type crystals. The melting behavior of these new compounds was investigated by thermogravimetric (TG) analysis and differential thermal analysis (DTA) using a SETARAM Setsys Evolution 18 analyzer. In this aim, powder from each synthesized compound was loaded into a platinum (Pt) crucible and heated in synthetic air flux (a mixture of 21%  $O_2$  and 79%  $N_2$  of 99.999% purity) to 1600 °C at a rate of 10 °C/min and then cooled to room temperature at the same rate. Figure 2 shows DTA curves corresponding to the  $La_{0.765}Y_{0.485}Sc_{2.75}(BO_3)_4$  compound. During the heating (blue curve), two endothermic peaks at 1473 °C and 1492 °C were present, indicating the melting of two compounds with ~1.4% mass loss. Similarly, two peaks at 1466 °C and 1357 °C arose during the cooling process (red curve in Figure 2) with a similar mass loss. Most likely, the mass losses were

mainly due to the continuous evaporation of  $B_2O_3$  (melting point of about  $450\text{ }^\circ\text{C}$ ). This behavior proves that compound  $La_{0.765}Y_{0.485}Sc_{2.75}(BO_3)_4$  has an incongruent melting. All investigated samples showed similar thermal behavior.

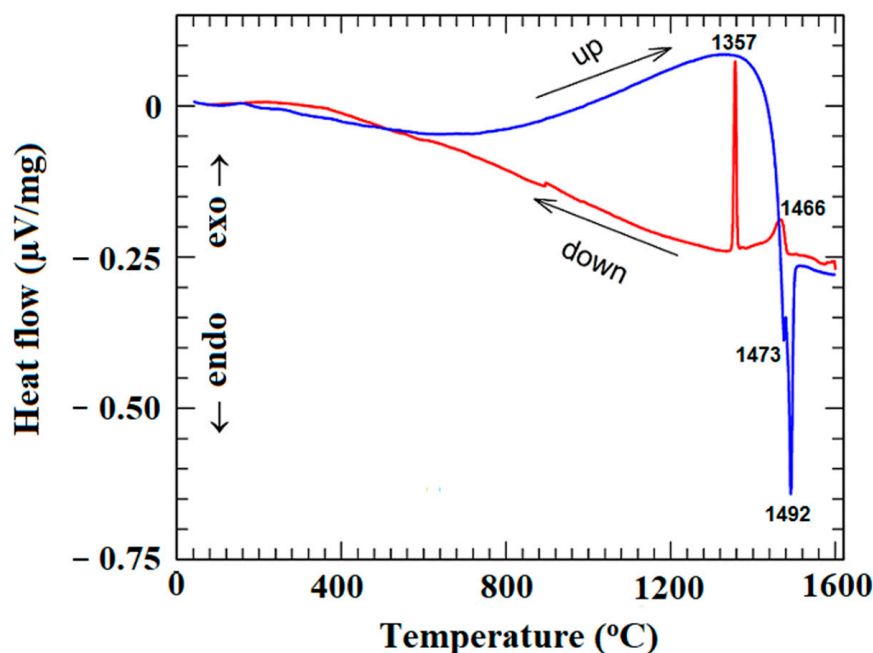


**Figure 2.** DTA analysis of  $La_{0.765}Y_{0.485}Sc_{2.75}(BO_3)_4$  nonstoichiometric compound. (Reprinted with permission from ref. [13], copyright 2019 American Chemical Society).

Compared to the growth of a congruent melting compound, the growth of an incongruent melting compound by the Czochralski method is more difficult and requires several supplementary precautions. Therefore, a special thermal setup shown in Figure 3 was developed for growing LYSB-type crystals by the Czochralski crystal growth method. The novelty of the thermal setup consists of the addition of two rings, one of ceramic  $Al_2O_3$  and the second of Pt, placed at a distance of approximately 20 mm and 2 mm, respectively, above the crucible, which act as baffles and have the main role of achieving a balance between the thermal gradients in the melt and the evaporation of  $B_2O_3$ , thus avoiding the constitutional supercooling phenomenon [5]. The high viscosity of the melt and its tendency to separate into different phases and to vitrify require intense stirring. This can be achieved by increasing the radial thermal gradients in the melt, which, at the same time, leads to its overheating and implicitly to an increase in the concentration of  $B_2O_3$  vapors above the melt. The condensation of  $B_2O_3$  vapors on the surface of the growing crystal is very harmful, because the liquid  $B_2O_3$  drains then into the high-temperature region and dissolves the growing crystal, thus leading to crystallization failure and even to the loss of contact between the melt and the growing crystal. In this respect, the developed thermal setup allows for efficient control of both the  $B_2O_3$  vapors' condensation on the growing crystal and the thermal gradients in the melt and over the crucible.

An ADL-MP crystal growth furnace equipped with a TruHeat MF 5030 induction heating generator (100 kHz) was used to grow LYSB-type crystals by the Czochralski technique. The growth experiments were performed using iridium (Ir) crucibles with a height of 30 mm and a diameter of 30 mm in a static atmosphere of  $N_2$  gas with 5N purity. In these conditions, five LYSB-type crystals were grown from melts with the initial compositions  $La_{0.754}Y_{0.546}Sc_{2.70}(BO_3)_4$ ,  $La_{0.7875}Y_{0.4625}Sc_{2.75}(BO_3)_4$ ,  $La_{0.8625}Y_{0.4375}Sc_{2.70}(BO_3)_4$ ,  $La_{0.8125}Y_{0.4375}Sc_{2.75}(BO_3)_4$ , and  $La_{0.765}Y_{0.485}Sc_{2.75}(BO_3)_4$ . Figure 4 shows the first four as-grown crystals. They were grown along the  $(001)$  direction using LGSB-oriented seeds and were of moderate quality, having a regular hexagonal shape typical of huntite-type crystals grown along the crystallographic  $c$ -axis [12]. As can be seen from Figure 4b, the crystal

grown from the melt with initial composition  $\text{La}_{0.7875}\text{Y}_{0.4625}\text{Sc}_{2.75}(\text{BO}_3)_4$  had a large transparent region inside the crystal body, which was very promising for cutting and obtaining crystal samples. During the growth of this crystal, the pulling rate used was 1.8 mm/h, and the rotation rate of the seed was kept constant at 10 rpm. However, when the crystal was tested for SHG of the fundamental wavelength 1064 nm, diffuse green radiation scattered in different directions was observed, thus indicating the existence of twinning defects, similar to the case of LYSB and YAB crystals grown by the flux method [15].

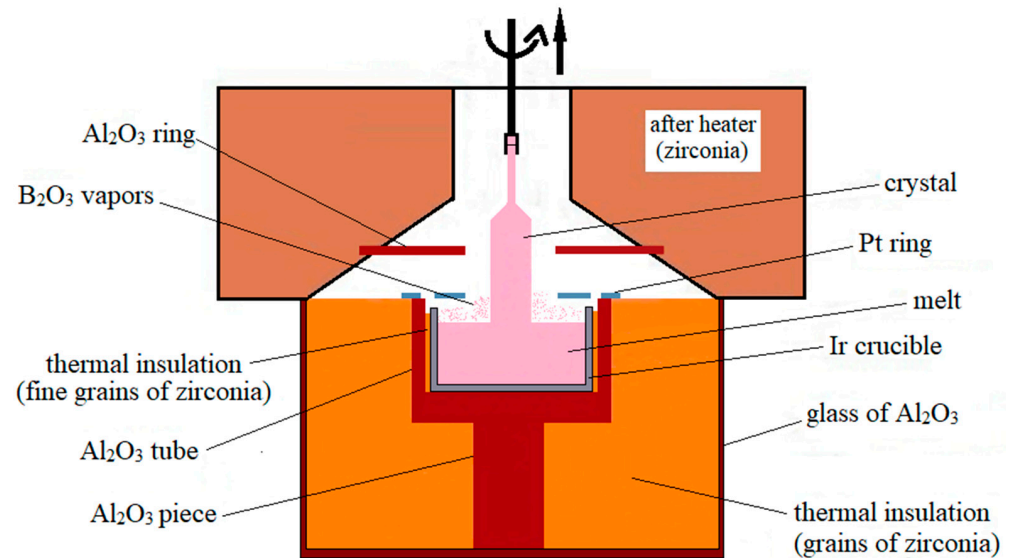


**Figure 3.** Thermal setup developed for growing LYSB-type crystals by the Czochralski crystal growth technique. (Reprinted with permission from ref. [13], copyright 2019 American Chemical Society).

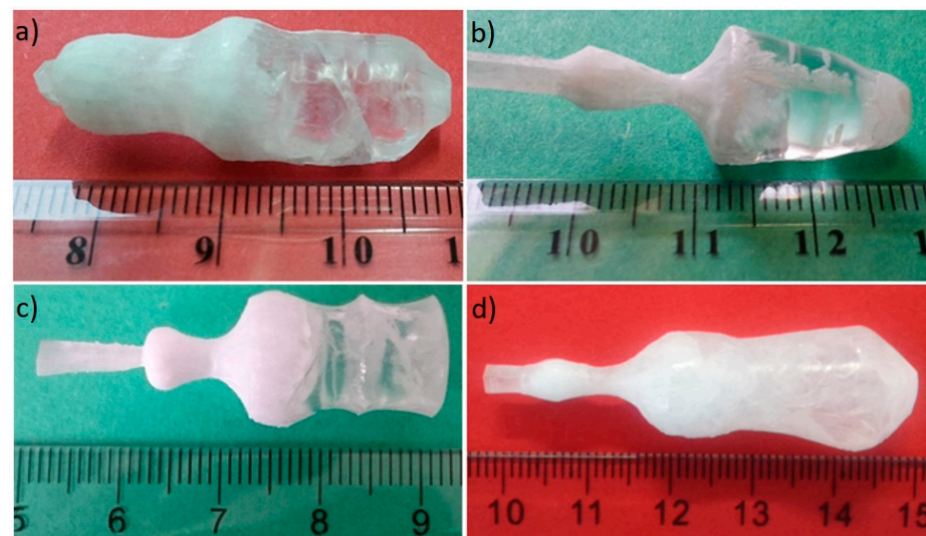


**Figure 4.** LYSB-type crystals grown from initial melts  $\text{La}_{0.754}\text{Y}_{0.546}\text{Sc}_{2.70}(\text{BO}_3)_4$  (a),  $\text{La}_{0.7875}\text{Y}_{0.4625}\text{Sc}_{2.75}(\text{BO}_3)_4$  (b),  $\text{La}_{0.8625}\text{Y}_{0.4375}\text{Sc}_{2.70}(\text{BO}_3)_4$  (c), and  $\text{La}_{0.8125}\text{Y}_{0.4375}\text{Sc}_{2.75}(\text{BO}_3)_4$  (d). (Reprinted with permission from ref. [13], copyright 2019 American Chemical Society).

A new crystal was grown from the initial melt with  $\text{La}_{0.765}\text{Y}_{0.485}\text{Sc}_{2.75}(\text{BO}_3)_4$  composition, a composition lying between the initial melt compositions (in terms of La/Y content) used to grow the LYSB crystals shown in Figure 4a,b. The as-grown crystal is shown in Figure 5. As can be observed, it had a high degree of transparency and was free of visible defects. Moreover, preliminary SHG tests of the 1064 fundamental wavelength confirmed the high quality of the grown crystal, the green radiation being generated only in the

phase-matching direction. In this case, too, the crystal was grown along the  $\langle 001 \rangle$  direction, using optimized rotation and pulling speeds of 8–10 rpm and 2 mm/h, respectively. Typically, in each crystal growth process, a maximum of ~15% of the initial melt mass (~90 g) was transformed into a single crystal. Similar to all grown crystals, the obtained crystal had typical dimensions of approximately 13 mm in diameter and 25 mm in length. Since the crystal grown from the initial melt composition  $\text{La}_{0.765}\text{Y}_{0.485}\text{Sc}_{2.75}(\text{BO}_3)_4$  had the best quality, the following investigations presented in this chapter were performed on this crystal.

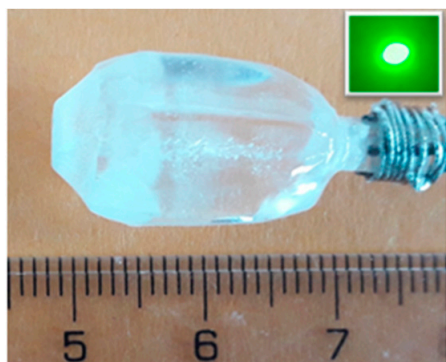


**Figure 5.** LYSB crystal grown from initial melt composition  $\text{La}_{0.765}\text{Y}_{0.485}\text{Sc}_{2.75}(\text{BO}_3)_4$ . The figure in the inset shows the LYSB crystal generating green light via SHG. (Reprinted with permission from ref. [13], copyright 2019 American Chemical Society).

The X-ray rocking curve (XRC) was measured on a laser-grade polished crystal sample oriented perpendicular to the  $c$ -axis ( $c$ -cut) using the same PANalytical Empyrean X-ray diffractometer. Figure 6 shows the XRC of the (003) reflection plane. The obtained peak had a symmetrical shape with a full width at half-maximum (FWHM) of  $0.013^\circ$ , indicating the good crystalline quality of the grown crystal. The laser-induced damage threshold (LDT) was measured using a pulsed Q-smart 850 Nd:YAG laser (1064 nm, 10 Hz, 6 ns). It was found that the LYSB crystal had a high LDT of  $\sim 2 \text{ GW}/\text{cm}^2$ , being four times larger compared to the value of  $0.4\text{--}0.6 \text{ GW}/\text{cm}^2$  obtained for the YAB crystal [4].

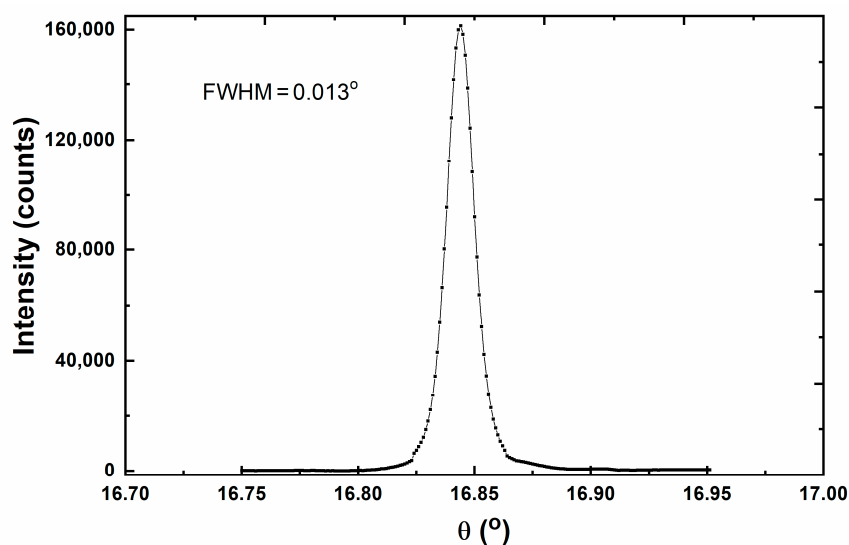


**Figure 6.** XRC of the LYSB crystal on the (003) diffraction plane. (Reprinted with permission from ref. [13], copyright 2019 American Chemical Society).

## 2.2. Structural and Compositional Characterization

The XRPD spectrum at room temperature of LYSB crystal is presented in Figure 7. The spectrum was very well indexed by the trigonal phase (space group  $R\bar{3}2$ , PDF card 04-018-1225), and no impurity phase was detected. The lattice constants were found to be  $a = 9.8098(4)$  Å and  $c = 7.9802(3)$  Å. Compared to the LYSB crystal grown by the flux method ( $a = 9.774(1)$  Å,  $c = 7.946(2)$  Å) [8], the LYSB crystal grown by the Czochralski technique had a larger unit cell.

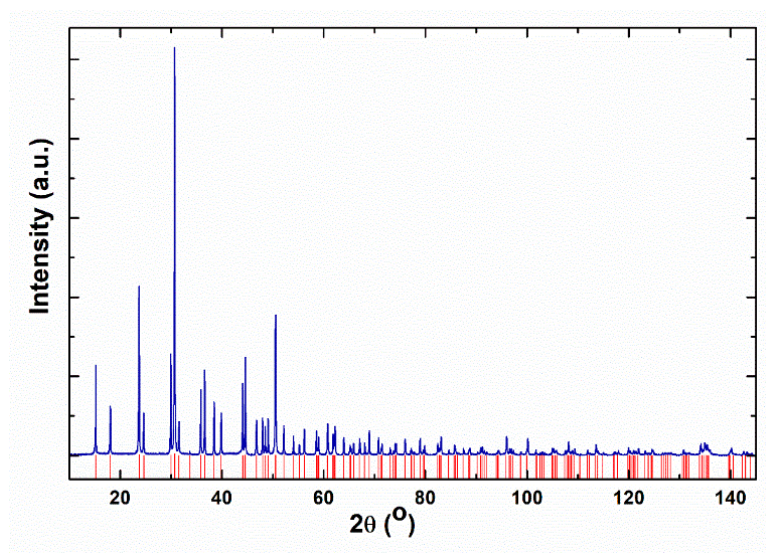


**Figure 7.** XRPD spectrum of LYSB crystal. The vertical sticks (in red color) correspond to PDF card 04-018-1225 of trigonal phase (space group  $R\bar{3}2$ ). (Reprinted with permission from ref. [13], copyright 2019 American Chemical Society).

The ICP-AES (inductively coupled plasma atomic emission spectrometry) method was used to determine the chemical composition of the grown crystal. A trace scan advantage spectrometer was employed. The compositional uniformity was evaluated using samples cut from different areas along the growth direction. Table 1 shows the chemical compositions of all measured samples. The crystal stoichiometry was determined according to the composition of the huntite-type compounds. Therefore, 4 B atoms and 12 O atoms were considered in each formula unit. As can be seen from Table 1, the crystal had a homogenous composition along the growth direction, and the chemical composition of LYSB crystal, with a measurement error of  $\pm 0.2\%$ , was determined to be  $\text{La}_{0.78}\text{Y}_{0.32}\text{Sc}_{2.90}(\text{BO}_3)_4$ . Considering the La/Y ratio (1.57 in the starting melt and over 2.40 in the grown crystal), we can deduce that the effective segregation coefficient of  $\text{Y}^{3+}$  ions in LSB matrix was less than one. Additionally, the La/Y ratio of over 2.40 in the grown crystal was higher than that of the flux-grown LYSB crystal of  $\sim 1.26$  [8]. From Table 1, it can also be observed that the stoichiometry of Sc cations is very close to 3 ( $\sim 2.90$ ) in the grown crystal, which implies that  $\text{Y}^{3+}$  ions largely substituted  $\text{La}^{3+}$  cations in the LYSB structure and that only a small fraction was inserted in the sites of  $\text{Sc}^{3+}$  cations.

**Table 1.** Chemical compositions of samples cut from different regions of the LYSB crystal. (Reprinted with permission from ref. [13], copyright 2019 American Chemical Society).

LYSB Crystal Sample		La/Y Ratio
Starting melt	$\text{La}_{0.765}\text{Y}_{0.485}\text{Sc}_{2.75}(\text{BO}_3)_4$	1.57
Shoulder	$\text{La}_{0.780}\text{Y}_{0.321}\text{Sc}_{2.899}(\text{BO}_3)_4$	2.42
Body	$\text{La}_{0.783}\text{Y}_{0.316}\text{Sc}_{2.901}(\text{BO}_3)_4$	2.47
Tail	$\text{La}_{0.779}\text{Y}_{0.324}\text{Sc}_{2.897}(\text{BO}_3)_4$	2.40

The LYSB crystal structure was refined using the Rietveld analysis according to XRPD data using the X'Pert High Score Plus software. During refinement, occupancy factors determined by elemental ICP analysis were used for the sites occupied by La and Sc cations. The obtained results are shown in Figure 8. The reliability parameters of the refinement were found to be  $R_p = 3.44$ ,  $R_{wp} = 4.42$ ,  $R_{exp} = 1.58$ , and  $GOF = 2.80$ , where  $R_p$ ,  $R_{wp}$ , and  $R_{exp}$  are the unweighted profile R-factor, the weighted profile R-factor, and the expected R-factor, respectively, and  $GOF$  is the goodness of fit. The atomic coordinates and site occupancy fraction after the Rietveld refinement are summarized in Table 2.

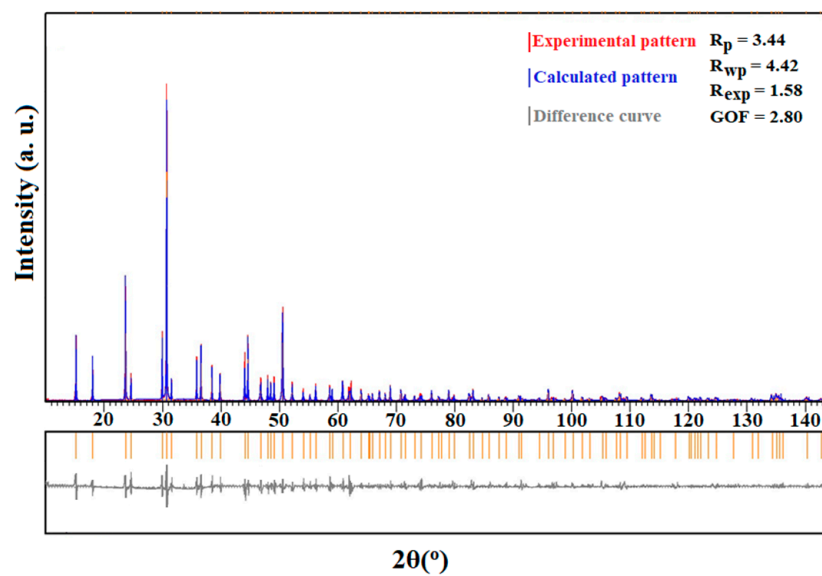


**Figure 8.** The experimental (in red), calculated (in blue), and difference (in grey) patterns after Rietveld analysis and refinement reliability parameters. (Reprinted with permission from ref. [13], copyright 2019 American Chemical Society).

**Table 2.** Atomic coordinates and site occupancy fraction in the LYSB crystal. (Reprinted with permission from ref. [13], copyright 2019 American Chemical Society).

Atom	x	y	z	Wyckoff Position	Occupancy
La	0	0	0	3a	0.78
Y1 (La)	0	0	0	3a	0.22
Sc	−0.1235	0.6666	0.6666	9d	0.9667
Y2 (Sc)	−0.1235	0.6666	0.6666	9d	0.0333
B1	−0.2317	0.6666	0.1666	9e	1
B2	0	0	0.5	3b	1
O1	0	−0.4177	0.5	9e	1
O2	−0.0263	0.1894	−0.2009	18e	1
O3	0	−0.1387	0.5	9e	1

The structure of LYSB crystal was visualized using VESTA software and is shown in Figure 9. It shows a typical huntite-type structure in which  $La^{3+}$  and a significant fraction of  $Y^{3+}$  ions (Y1 in Figure 9) are located in the trigonal prismatic sites with  $D_3(32)$  symmetry and have six-fold oxygen coordination. The  $BO_3$  triangles are distributed in almost planar layers separating these prisms, and, therefore, the  $La(Y)O_6$  trigonal prisms are completely isolated from one another. The  $Sc^{3+}$  and a small fraction of  $Y^{3+}$  ions (Y2 in Figure 9) are located in the octahedral sites with  $C_2(2)$  symmetry, forming distorted octahedra with shared edges.

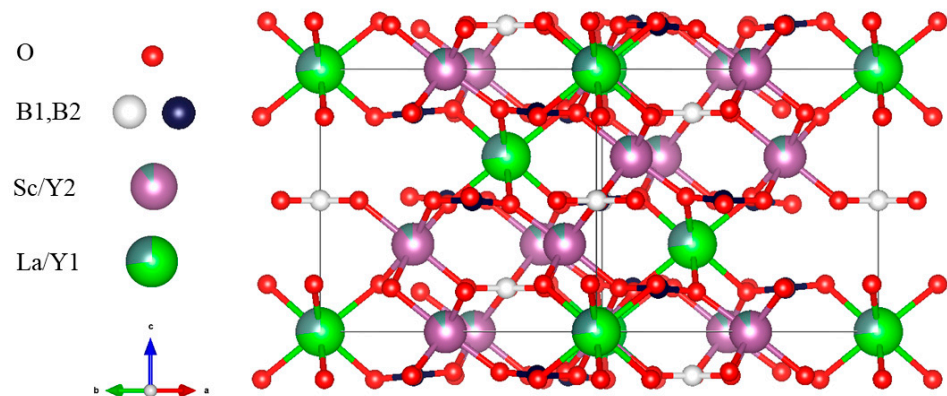


**Figure 9.** LYSB crystal structure. (Reprinted with permission from ref. [13], copyright 2019 American Chemical Society).

### 2.3. Optical and Vibrational Characterization

The optical transmission spectrum of the LYSB crystal was registered at room temperature on a 1.75 mm thick *c*-cut crystal sample using a Varian Cary 5000 UV-Vis-NIR spectrophotometer. As shown in Figure 10, the LYSB crystal had a wide optical transparency window with a high transmittance of over 80% in the wavelength range of 400–2450 nm. No absorption peaks were detected in this wavelength range, and the UV cut-off wavelength was below 200 nm (the lower limit of the spectrophotometer). Compared to the LGSB crystal grown by the Czochralski method [12], which has a UV cut-off wavelength of 230 nm and some absorption peaks in the UV range due to the absorption of  $Gd^{3+}$  ions, the LYSB crystal is more suitable for use in various NLO devices in the UV domain. The energy band gap was calculated from Tauc's plot (the inset of Figure 10) as  $E_g = 6.0$  eV, close to the value of 5.7 eV reported for the YAB crystal [16].

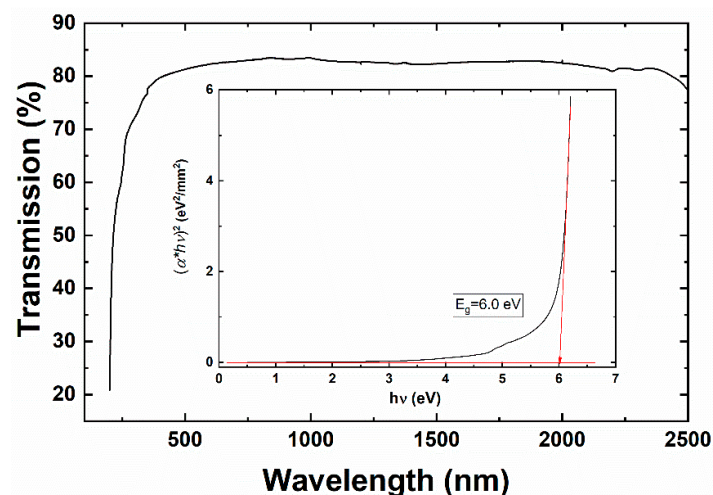


**Figure 10.** Optical transparency window of the LYSB crystal. Tauc's plot is shown in the figure inset. (Adapted with permission from ref. [13], copyright 2019 American Chemical Society).

The Raman spectrum of the LYSB crystal was also registered at room temperature under the laser excitation wavelength of  $\lambda = 633$  nm on the same 1.75 mm thick oriented crystal sample. The obtained spectrum is shown in Figure 11. The maximum phonon energy was found to be  $\sim 1283$   $cm^{-1}$ , lower than the values determined for the YAB ( $>1400$   $cm^{-1}$ ) and Czochralski-grown Pr:LGSB ( $\sim 1414$   $cm^{-1}$ ) crystals [17,18].

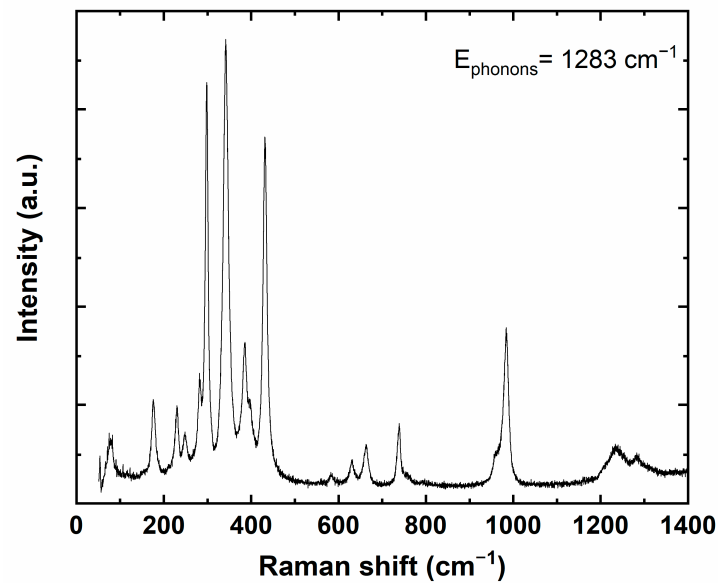


**Figure 11.** Raman spectrum of the LYSB crystal.

#### 2.4. NLO Properties

The refractive indices of the LYSB crystal were measured by the minimum deviation technique using a ZEISS optical goniometer. For this purpose, a prism having the prism axis parallel to the Z-axis and an apex angle of  $60^{\circ}28'$  was cut from the LYSB crystal, and the entrance and exit faces of the light through the prism were well polished (Figure 12). Different gas-discharge lamps (Zn, Hg, Na, Cd) with emission in the visible domain and some laser diodes with emissions at 974 nm (Limo, Dortmund, Germany) and at 877 and 808 nm (Coherent, Santa Clara, CA, USA) were used as light sources.

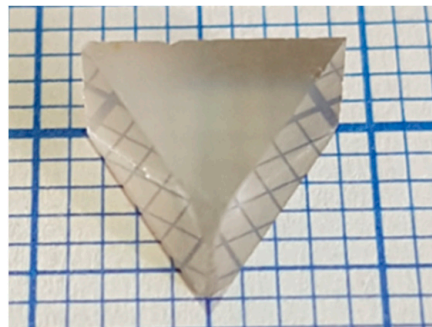


**Figure 12.** Prism for measuring the refractive indices of the LYSB crystal. (Reprinted with permission from ref. [13], copyright 2019 American Chemical Society).

The values of the ordinary ( $n_o$ ) and extraordinary ( $n_e$ ) refractive indices as a function of wavelength are summarized in Table 3. The birefringence ( $\Delta n$ ) is also presented. As can be seen in Table 3, LYSB is an optically negative uniaxial crystal, as  $n_e < n_o$ .

The dispersion of the refractive indices was fitted by the least-squares method, using the following Sellmeier equation [19]:

$$n_i^2(\lambda) = A + \frac{B}{\lambda^2 - C} - D\lambda^2 \quad (1)$$

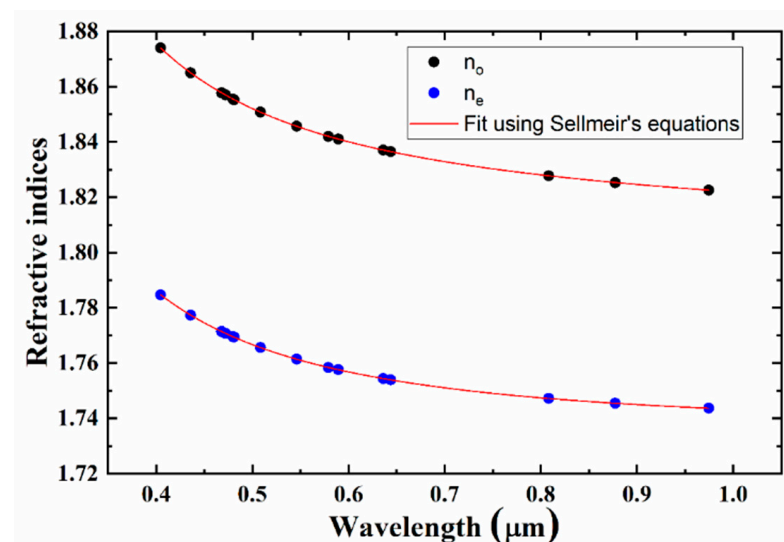
where  $i$  denotes the ordinary (o) or extraordinary (e) indices;  $\lambda$  is the wavelength expressed in  $\mu\text{m}$ ; and A, B, C, and D are the Sellmeier coefficients (listed in Table 4). Figure 13 shows the dispersion curves of the refractive indices along with the fit of the experimental data.

**Table 3.** LYSB crystal refractive indices. (Adapted with permission from ref. [13], copyright 2019 American Chemical Society).

Wavelength ( $\mu\text{m}$ )	$n_o$		$n_e$		$\Delta n$	
	Measured	Calculated	Measured	Calculated	Measured	Calculated
0.40466	1.8740	1.8739	1.7847	1.7846	0.0893	0.0893
0.43584	1.8650	1.8649	1.7773	1.7772	0.0877	0.0877
0.46782	1.8578	1.8578	1.7714	1.7713	0.0864	0.0865
0.46801	1.8578	1.8577	1.7714	1.7713	0.0864	0.0864
0.47222	1.8570	1.8569	1.7707	1.7706	0.0863	0.0863
0.47999	1.8555	1.8554	1.7695	1.7694	0.086	0.086
0.48105	1.8553	1.8552	1.7694	1.7692	0.0859	0.086
0.50858	1.8508	1.8507	1.7656	1.7655	0.0852	0.0852
0.54607	1.8457	1.8456	1.7614	1.7613	0.0843	0.0843
0.57906	1.8420	1.8420	1.7584	1.7584	0.0836	0.0836
0.5893	1.8411	1.8410	1.7576	1.7575	0.0835	0.0835
0.63623	1.8371	1.8370	1.7544	1.7543	0.0827	0.0827
0.64385	1.8365	1.8365	1.7539	1.7539	0.0826	0.0826
0.8082	1.8278	1.8277	1.7472	1.7471	0.0806	0.0806
0.8773	1.8253	1.8253	1.7455	1.7454	0.0798	0.0799
0.9745	1.8226	1.8226	1.7437	1.7436	0.0789	0.079

**Table 4.** Sellmeier coefficients of the LYSB crystal.

Sellmeier Coefficients	Refractive Index	
	$n_o^2$	$n_e^2$
A	3.30146	3.01189
B	0.03004	0.02536
C	0.02237	0.01722
D	0.0127	−0.0014

**Figure 13.** Variation of refractive indices with wavelength in the LYSB crystal. (Reprinted with permission from ref. [13], copyright 2019 American Chemical Society).

Based on the measured refractive indices and the Sellmeier equations, type-I and type-II phase-matching curves for LYSB were determined and are presented in Figure 14. The LYSB crystal was type-I and -II phase-matchable over a broad range of fundamental wavelengths. The SHG phase-matching lower limit was at the fundamental wavelength of 579 nm, being higher than that reported for the YAB crystal of 490 nm. Thus, the shortest

wavelength obtainable by SHG was 289 nm. Regarding the type-I SHG of the 1064 nm fundamental wavelength, the value of the phase-matching angle was determined to be  $\theta_{pm} = 33.4^\circ$ , being close to the value of  $\theta_{pm} = 33.5^\circ$  found for the LYSB crystal grown by the flux method [7,8]. Moreover, 355 nm UV radiation may be generated in Czochralski-grown LYSB crystal by using type-II sum frequency generation (SFG, eoe) of the fundamental wavelengths of 532 and 1064 nm at  $\theta_{pm} = 65.2^\circ$  (Figure 15).

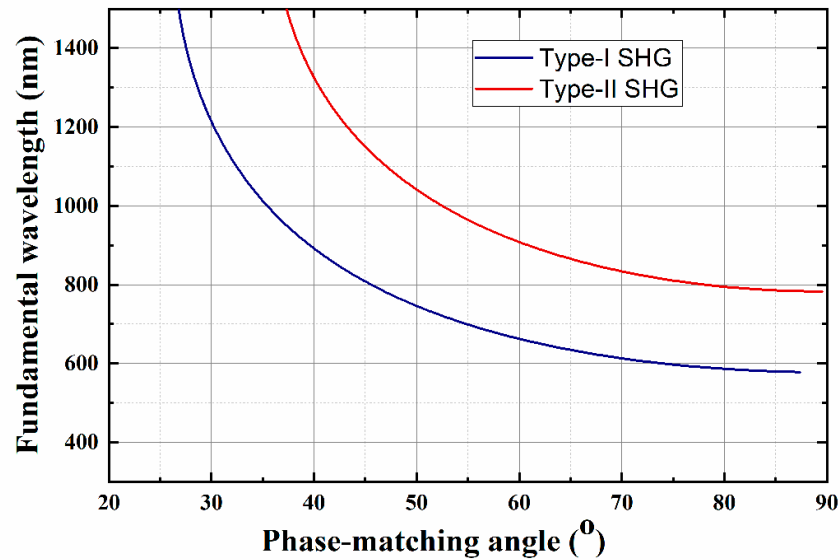


Figure 14. Phase-matching curves for SHG of types I and II in the LYSB crystal. (Reprinted with permission from ref. [13], copyright 2019 American Chemical Society).

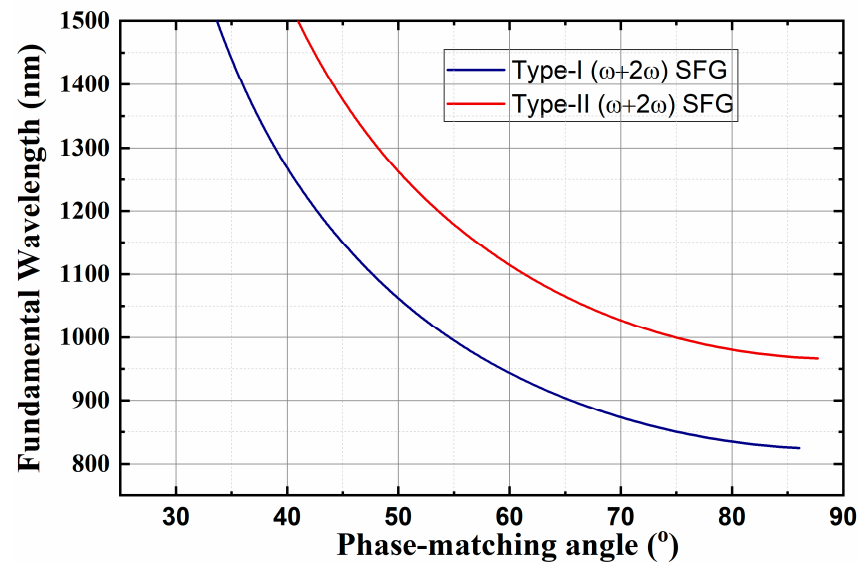


Figure 15. Phase-matching curves for SFG of types I and II in the LYSB crystal. (Reprinted with permission from ref. [13], copyright 2019 American Chemical Society).

The spectral acceptance ( $\Delta\lambda \times L$ ), angular acceptance ( $\Delta\theta \times L$ ), and walk-off angle ( $\rho$ ) were determined using the following equations [20–22]:

$$\Delta\lambda \times L = 0.443 \left( \frac{dn_o}{d\lambda}(\lambda_F) - \frac{1}{2} \frac{dn_e}{d\lambda}(\lambda_{SH}) \right)^{-1} \quad (2)$$

$$\Delta\theta \times L = 0.443\lambda \left[ \frac{1 + \frac{n_o^2(2\omega)}{n_e^2(2\omega)} \tan^2(\theta)}{\tan(\theta) \left| 1 - \left( \frac{n_o(2\omega)}{n_e(2\omega)} \right)^2 \right| n_e(2\omega, \theta)} \right] \quad (3)$$

$$\tan \rho = \frac{1}{2} [n_o(\omega)]^2 \left\{ \frac{1}{[n_e(2\omega)]^2} - \frac{1}{[n_o(2\omega)]^2} \right\} \sin 2\theta \quad (4)$$

where  $\lambda_F$  and  $\lambda_{SH}$  are the wavelengths of the fundamental and second harmonic radiation, respectively;  $L$  is the length of the crystal;  $\theta$  is the phase-matching angle; and  $n_e(2\omega)$ ,  $n_o(2\omega)$ , and  $n_o(\omega)$  are the extraordinary (e) and ordinary (o) refractive indices for second harmonic and fundamental frequencies. The LYSB crystal has only two non-zero independent nonlinear coefficients,  $d_{11}$  and  $d_{14}$ , assuming Kleinman symmetry relations. Since  $d_{14}$  has no contribution in the case of type-I SHG, only  $d_{11}$  is considered in further calculations. Therefore, the effective nonlinear coefficient can be estimated using the following relation [23]:

$$d_{eff}^{type\ I} = d_{11} \cos\theta \cos 3\varphi \quad (5)$$

where  $\theta$  and  $\varphi$  are phase-matching angles for type-I SHG. More exactly,  $\theta$  is defined as the angle between the crystallophysic  $Z$  axis and the direction of propagation through the crystal, and  $\varphi$  is the angle between the crystallophysic  $X$  axis and the projection of the direction of propagation in the  $XY$  plane of the crystal (Figure 16).

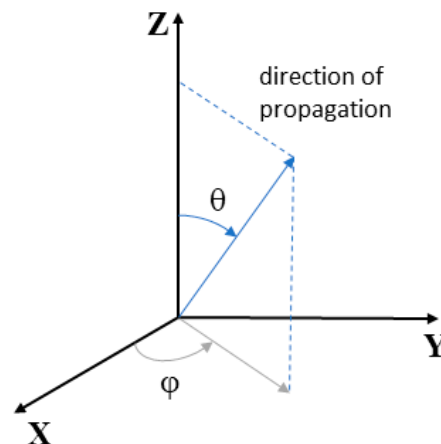


Figure 16. Definition of the phase-matching angles  $\theta$  and  $\varphi$ .

Based on the anionic group theory [2], the magnitude of the  $d_{11}$  nonlinear coefficient can be calculated using the following equation [7]:

$$d_{11} = \frac{F}{V} \sum_{p=1}^N \sum_{ijk} R_{1i} R_{1j} R_{1k} \beta_{ijk} \quad (6)$$

where  $F$  is the local-field factor;  $V$  represents the unit-cell volume;  $R_{1x}$  denotes the orientation direction cosine for each  $\text{BO}_3$  group; and  $\beta_{ijk}$  is the component of the hyperpolarizability tensor for each  $\text{BO}_3$  anionic group with only one non-zero component,  $\beta_{111}$ . The values of  $(\theta, \varphi)$ ,  $\Delta n$ ,  $\rho$ ,  $\Delta\theta \times L$ ,  $\Delta\lambda \times L$ , and  $d_{11}$  for type-I SHG of the fundamental wavelength of 1064 nm are listed in Table 5.

**Table 5.** NLO properties of the Czochralski-grown LYSB crystal for type-I SHG of 1064 nm fundamental wavelength. (Adapted with permission from ref. [13], copyright 2019 American Chemical Society).

Crystal	( $\theta, \varphi$ ) (deg)	$\Delta n$ @1064 (nm)	$\rho$ (deg)	$\Delta\theta \times L$ (deg·cm)	$\Delta\lambda \times L$ (nm·cm)	$d_{11}$ (pm/V)
LYSB	(33.4, 60)	0.078	2.41	0.034	0.60	1.35

Presently, the most well-known SHG crystals commonly used for the manufacture of various laser systems include NLO crystals such as  $YAl_3(BO_3)_4$  (YAB),  $LiB_3O_5$  (LBO),  $\beta$ - $BaB_2O_4$  (BBO),  $Li_2B_4O_7$ ,  $CsLiB_6O_{10}$  (CLBO),  $KTiOPO_4$  (KTP),  $KH_2PO_4$  (KDP),  $LiNbO_3$ , and  $KNbO_3$ . A summary of their main properties ( $d_{eff}$ , phase-matching angles, transparency window, laser-induced damage threshold, crystal growth method, and some comments) for SHG of fundamental emission at 1064 nm compared to those of the LYSB crystal grown by the Czochralski method is presented in Table 6.

**Table 6.** NLO properties for SHG of 1064 nm fundamental emission in selected NLO crystals [4,13,19,24–43].

Crystal	$d_{eff}$ (pm/V)	$\theta$ Phase-Matching (deg)	Phase-Matching Type	Optical Transparency Window (nm)	LDT* (J/cm <sup>2</sup> )	Growth Method	Comments
LYSB <i>this work</i>	1.13	33.4	I	200–2800	20	Czochralski	
YAB	1.45	30.8	I	170–2800	4–6	Flux	
$LiB_3O_5$ (LBO)	1.17	$\theta = 90$ $\varphi = 0 @150^\circ C$	biaxial	160–2600	25	Flux	
$B-BaB_2O_4$ (BBO)	2.01 1.43	22.8 32.3	I II	198–2600	13	Flux	
$Li_2B_4O_7$	0.07	30.5	I	160–3500	40	Czochralski	soluble in water
$CsLiB_6O_{10}$ (CLBO)	0.49 0.95	29.2 42.1	I II	170–2600	25	Flux	hygroscopic
$KTiOPO_4$ (KTP)	3.24	$\theta = 90$ $\varphi = 22.81$	biaxial	350–4500	15	Flux	
$KH_2PO_4$ (KDP)	0.26 0.34	42.0 58.6	I II	177–1700	10	Flux	soluble in water
$LiNbO_3$		not phase-matchable @ 1064 nm		330–5500	14	Czochralski	
$KNbO_3$	10.90	$\theta = 90$ $\varphi = 90$ @188 °C	biaxial	400–4500	1.7	Czochralski	

\*  $\tau_p = 10$  ns,  $\lambda = 1064$  nm.

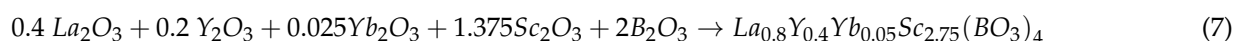
The main disadvantage of YAB, LBO, BBO, CLBO, KTP, and KDP crystals is that they can be obtained only by the flux crystal growth method, which involves complex and long-time growth processes as well as some limitations in the size and optical quality of the grown crystals. For example, in the case of YAB crystal, different flux components, such as Fe or Mo, are present as impurities, leading to the appearance of some absorption bands that limit its applications in the UV spectral range. LBO is currently the most widely used crystal for high-power SHG of 1064 nm radiation due to its high LDT and non-critical phase-matching. However, it is not phase-matchable for fundamental wavelengths shorter than 688 nm, which limits its functionality in obtaining near-UV radiation. BBO crystal presents both type-I and type-II phase-matching for a large range of fundamental radiations, with the shortest fundamental type-I phase-matched wavelength of 410 nm. The limitations of BBO are the difficulty of growing crystals of consistent quality and very high phase-matching angular sensitivity, thus requiring great precision and a very small tolerance regarding the positioning of the crystal into the system.  $Li_2B_4O_7$ , CLBO, and KDP crystals have water solubility problems and, thus, require much attention in handling, packaging, and especially in use. Moreover, they all have low values of  $d_{eff}$ . As for the KTP,  $LiNbO_3$ , and  $KNbO_3$  crystals, they possess high values of  $d_{eff}$  but are not optically transparent in the UV range. As can be seen from Table 6, the Czochralski-grown LYSB

crystal has an effective nonlinear coefficient,  $d_{\text{eff}} = 1.13 \text{ pm/V}$ , almost identical to that of LBO crystal ( $1.17 \text{ pm/V}$ ); it is type-I phase-matchable at  $1064 \text{ nm}$  ( $\theta_{\text{pm}} = 33.4^\circ$ ); possesses a large transparency window in the range of  $200\text{--}2800 \text{ nm}$ , slightly larger than that of LBO crystal ( $198\text{--}2600 \text{ nm}$ ); has a high laser-induced damage threshold,  $\text{LDT} = 20 \text{ J/cm}^2$ , close to that of LBO and CLBO crystals of  $20 \text{ J/cm}^2$ ; and, last but not least, it can be obtained in large dimensions and excellent optical quality by the Czochralski technique. Taking into account all of these favorable properties, it can be assumed that Czochralski-grown LYSB crystals constitute a new class of highly efficient crystals for different NLO applications, including SHG of high-power or high-energy laser beams.

### 3. Yb-Doped $\text{La}_x\text{Y}_y\text{Sc}_{4-x-y}(\text{BO}_3)_4$ Crystal

#### 3.1. Material Synthesis and Czochralski Growth

In order to be used as starting compound (initial melt composition) for growth by the Czochralski method, the polycrystalline compound LYSB:Yb was synthesized by using the same procedure as for the undoped LYSB crystal. Oxide powders of 5N purity ( $\text{La}_2\text{O}_3$ ,  $\text{Y}_2\text{O}_3$ ,  $\text{Yb}_2\text{O}_3$ , and  $\text{Sc}_2\text{O}_3$ ) and 99.98%  $\text{B}_2\text{O}_3$  were used as raw materials. The  $\text{Yb}^{3+}$  ions' doping concentration in the LYSB host matrix was selected to be 5 at.% with respect to the nonstoichiometric  $(\text{La}_{1-x}\text{Y}_x)_{1.25}\text{Sc}_{2.75}(\text{BO}_3)_4$  undoped compounds. Consequently, the raw materials were weighed according to the following chemical reaction:



LYSB:Yb single crystal was grown by the Czochralski method using the same thermal setup as for the undoped crystal. A  $\langle 001 \rangle$  oriented LYSB seed was used to initiate the growth, and the pulling rate was set at  $2 \text{ mm/h}$ , while the seed rotation varied between 8 and 10 rpm during the growth process. Figure 17 shows the as-grown LYSB:Yb crystal. As can be seen, the crystal was of excellent quality, being very transparent and without any visible defects. Moreover, the quality of the LYSB:Yb crystal appeared to be higher than that of the undoped LYSB crystal, which could be attributed to a better choice of the initial melt composition used to grow the LYSB:Yb crystal. The dimensions of the grown crystal were  $35 \text{ mm}$  in length and  $12 \text{ mm}$  in diameter. Preliminary SHG tests of the  $1064 \text{ nm}$  fundamental wavelength confirmed the high quality of the grown crystal, the green radiation being generated only in the phase-matching direction, thus indicating the absence of twinning defects existing in flux-grown LYSB and YAB crystals [15] or in LYSB crystals grown by the Czochralski method from inappropriate initial melt compositions.

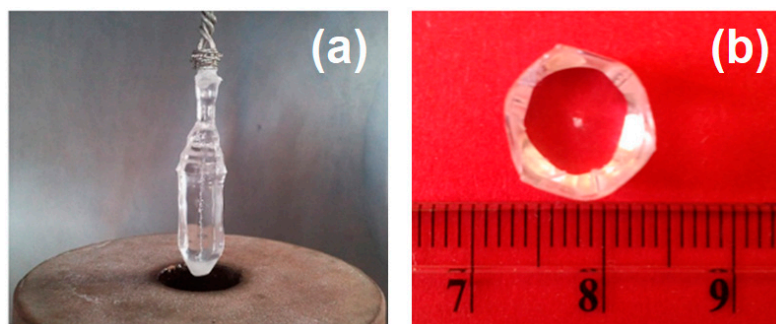


**Figure 17.** Photo of the as-grown LYSB:Yb crystal (a) and the cross-section of the crystal (b). Reprinted with permission from ref. [44], copyright 2020, Elsevier.

The XRPD spectrum of the LYSB:Yb crystal was recorded at room temperature using the same PANalytical Empyrean X-ray diffractometer ( $\lambda = 1.5406 \text{ \AA}$ ). The measured spectrum is presented in Figure 18 along with the PDF card 04-015-9641 of the  $\text{La}_{0.78}\text{Gd}_{0.22}\text{Sc}_3(\text{BO}_3)_4$  (LGSB) crystal (trigonal structure, space group  $R\bar{3}2$  [10]). All diffraction peaks were very well indexed by the huntite-type structure of pure LGSB crystal. The

lattice constants were determined as  $a = 9.8114(4) \text{ \AA}$  and  $c = 7.9808(9) \text{ \AA}$ , being slightly higher than for the undoped LYSB crystal ( $a = 9.8098(4) \text{ \AA}$  and  $c = 7.9802(3) \text{ \AA}$ ) [13].

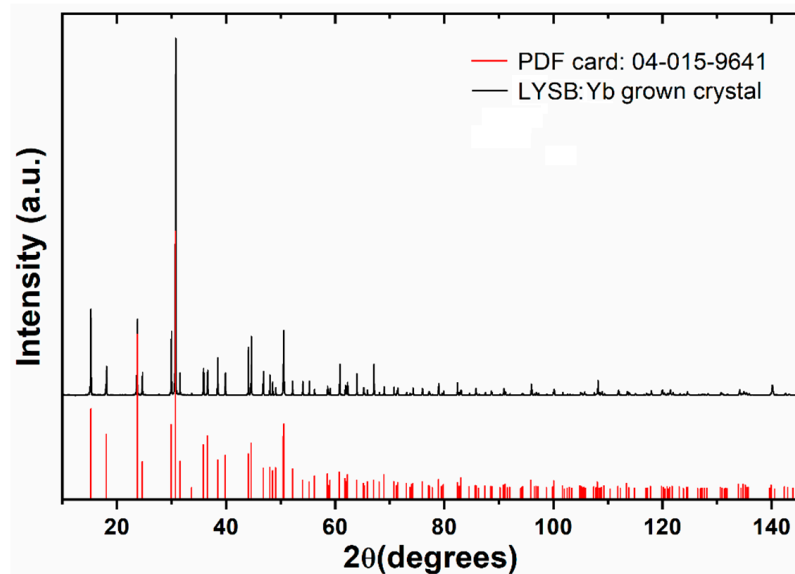


**Figure 18.** XRPD spectrum of LYSB:Yb crystal (black line) together with PDF card 04-015-9641 (red sticks) of LGSB crystal. Reprinted with permission from ref. [44], copyright 2020, Elsevier.

The ICP-AES method was employed to evaluate the chemical uniformity and determine the elemental composition of the as-grown crystal. Table 7 summarizes the chemical compositions of different samples cut from the grown crystal. The small compositional variation along the growth direction indicates good compositional uniformity, and the composition of the grown crystal was determined as being  $\text{La}_{0.78}\text{Y}_{0.32}\text{Yb}_{0.04}\text{Sc}_{2.86}(\text{BO}_3)_4$ , indicating a doping concentration of  $\text{Yb}^{3+}$  ions in the grown LYSB:Yb crystal of 4 at.%, i.e., LYSB:Yb (4 at.%). Taking into account that the concentration of  $\text{Yb}^{3+}$  ions in the starting melt was 5 at.%, the effective segregation coefficient ( $k_{\text{eff}}$ ) of  $\text{Yb}^{3+}$  ions was determined to be  $k_{\text{eff}} = 0.8$ . It can also be observed that the Sc content was lower than in the undoped LYSB crystal, which means that  $\text{Yb}^{3+}$  ions substituted both RE (RE = La, Y) and Sc sites in the LYSB:Yb (4 at.%) crystal structure.

**Table 7.** Chemical compositions of samples cut from different regions of LYSB:Yb (4 at.%) crystal. Reprinted with permission from ref. [44], copyright 2020, Elsevier.

starting melt	$\text{La}_{0.8}\text{Y}_{0.4}\text{Yb}_{0.05}\text{Sc}_{2.75}(\text{BO}_3)_4$
shoulder	$\text{La}_{0.780}\text{Y}_{0.320}\text{Yb}_{0.040}\text{Sc}_{2.860}(\text{BO}_3)_4$
body	$\text{La}_{0.778}\text{Y}_{0.322}\text{Yb}_{0.042}\text{Sc}_{2.858}(\text{BO}_3)_4$
tail	$\text{La}_{0.775}\text{Y}_{0.325}\text{Yb}_{0.042}\text{Sc}_{2.858}(\text{BO}_3)_4$

### 3.2. Evaluation of NLO Properties

The refractive indices of the LYSB:Yb (4 at.%) crystal were also measured using the minimum deviation method. The measured refractive indices (Table 8) were fitted according to the Sellmeier equations:

$$n_o^2(\lambda) = 3.3124 + \frac{0.0296}{\lambda^2 - 0.0192} - 0.0262\lambda^2 \quad (8)$$

$$n_e^2(\lambda) = 3.0254 + \frac{0.0239}{\lambda^2 - 0.0179} - 0.0159\lambda^2 \quad (9)$$

**Table 8.** Refractive indices of LYSB:Yb (4 at.%) crystal. Reprinted with permission from ref. [45], copyright 2020, Elsevier.

Wavelength (μm)	n <sub>e</sub>		n <sub>o</sub>	
	Calculated	Measured	Calculated	Measured
0.40466	1.7852	1.7851	1.8744	1.8744
0.43584	1.7780	1.7783	1.8658	1.8656
0.46782	1.7723	1.7725	1.8589	1.8590
0.46801	1.7723	1.7720	1.8588	1.8589
0.47222	1.7716	1.7715	1.8580	1.8583
0.47999	1.7704	1.7701	1.8566	1.8564
0.48105	1.7703	1.7702	1.8564	1.8565
0.50858	1.7665	1.7669	1.8519	1.8522
0.54607	1.7624	1.7626	1.8469	1.8466
0.57906	1.7594	1.7590	1.8432	1.8429
0.63623	1.7552	1.7552	1.8381	1.8379
0.64385	1.7547	1.7548	1.8376	1.8377
0.8082	1.7472	1.7474	1.8281	1.8284
0.8773	1.7450	1.7447	1.8253	1.8255
0.9745	1.7424	1.7424	1.8219	1.8217

Figure 19 shows the wavelength dispersion of the refractive indices together with the Sellmeier fit. The values of the refractive indices of the LYSB:Yb (4 at.%) crystal were determined to be very close to those of undoped LYSB crystal. Therefore, the phase-matching properties for type-I and type-II SHG and SFG are also similar.

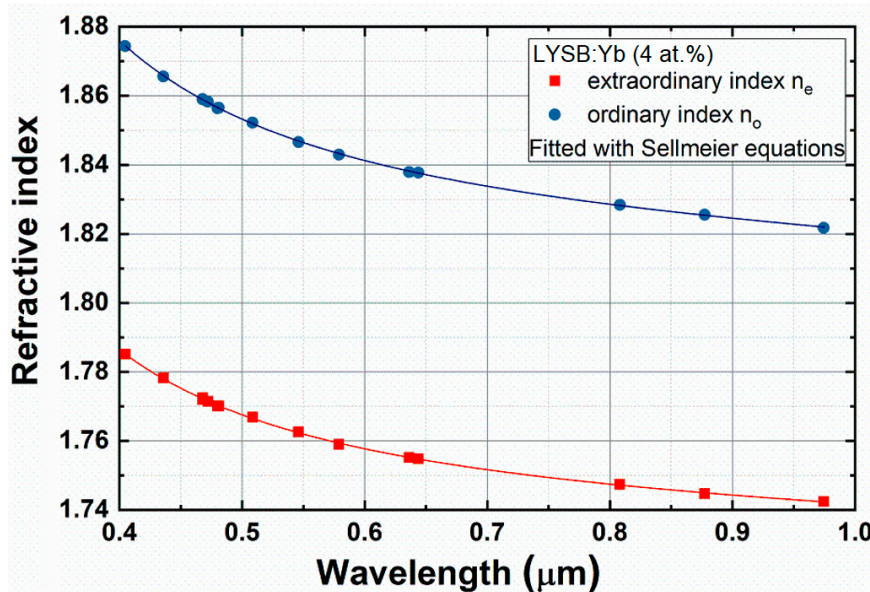


**Figure 19.** Variation of refractive indices with wavelength in the LYSB:Yb (4 at.%) crystal. Reprinted with permission from ref. [44], copyright 2020, Elsevier.

The values of  $(\theta, \varphi)$ ,  $(\rho)$ ,  $(\Delta\theta \times L)$   $(\Delta\lambda \times L)$ , and  $(d_{\text{eff}})$  for SHG of type I of the fundamental wavelength of 1028 nm were determined and are reported in Table 9.

**Table 9.** NLO properties for SHG of type I of the fundamental wavelength of 1028 nm in LYSB:Yb (4 at.%) crystal. Reprinted with permission from ref. [44], copyright 2020, Elsevier.

LYSB:Yb 1028 nm → 514 nm	$(\theta, \varphi)$ (deg)	$d_{\text{eff}}$ (pm/V)	$\Delta\lambda \times L$ (nm × cm)	$\Delta\theta \times L$ (deg × cm)	$\rho$ (deg)
	(36.0, 60)	1.09	0.74	0.031	2.53

### 3.3. Spectroscopic Properties

The spectroscopic properties of  $\text{Yb}^{3+}$  ions were evaluated to investigate the laser emission characteristics of the LYSB:Yb (4 at.%) crystal as a new laser material. Figure 20 presents the optical transmission spectrum in the range of 220–2500 nm recorded at room temperature using a Varian Cary 5000 UV-VIS-NIR spectrophotometer on a 1.0 mm thick *c*-cut crystal sample. The LYSB:Yb crystal had a high transparency of about 80% in both VIS and NIR spectral ranges, which is an essential property required to achieve efficient direct NIR laser emission or in the VIS range via SHG or self-frequency doubling processes. The only absorption lines observed in the spectrum were located in the 900–1000 nm range and corresponded to the  ${}^2\text{F}_{7/2} \rightarrow {}^2\text{F}_{5/2}$  intraconfigurational absorption transition of  $\text{Yb}^{3+}$  ions. Compared to the undoped LYSB crystal, the cut-off wavelength of the transmission spectrum was red-shifted by 20 nm, having a value of 220 nm. Taking into account that  $\text{Yb}^{3+}$  ions may substitute both  $\text{RE}^{3+}$  ( $\text{RE} = \text{La}, \text{Y}$ ) and  $\text{Sc}^{3+}$  ions, we can attribute this shift to the modification of the contents of RE and Sc cations in the LYSB host matrix induced by doping with  $\text{Yb}^{3+}$  ions. Compared to the isostructural LGSB:Yb crystal [46], LYSB:Yb had a higher transmission and also showed no absorption lines in the UV spectral range specific to  $\text{Gd}^{3+}$  ions, thus being more advantageous for NLO applications, particularly in the UV domain.

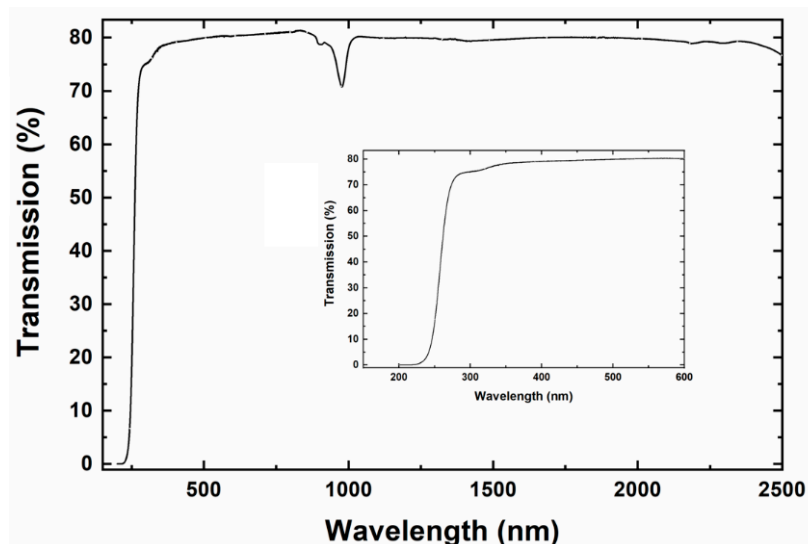
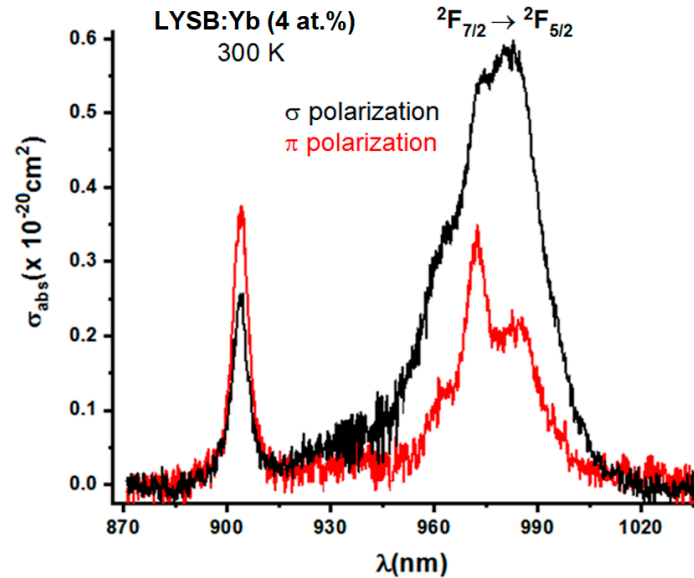


**Figure 20.** Transmission spectrum of LYSB:Yb (4 at.%) crystal. The inset figure presents the transmission over UV and VIS wavelength ranges. Reprinted with permission from ref. [44], copyright 2020, Elsevier.

The room-temperature (300 K) and low-temperature (10 K) absorption and emission spectra of the LYSB:Yb (4 at.%) crystal were recorded in polarized light on a 0.93 mm thick crystal sample oriented perpendicular to the *a*-axis direction (*a*-cut). The detection system consisted of a Jarell Ash monochromator equipped with an S1 photomultiplier or Ge photodiode coupled to a lock-in amplifier and connected to a computer. As excitation sources, a halogen lamp (for absorption spectra) and an OPO laser OPOTEK RADIANT 355 LD (for emission spectra) were used. A closed-cycle He refrigerator ARS-2HW was used for low-temperature measurements.

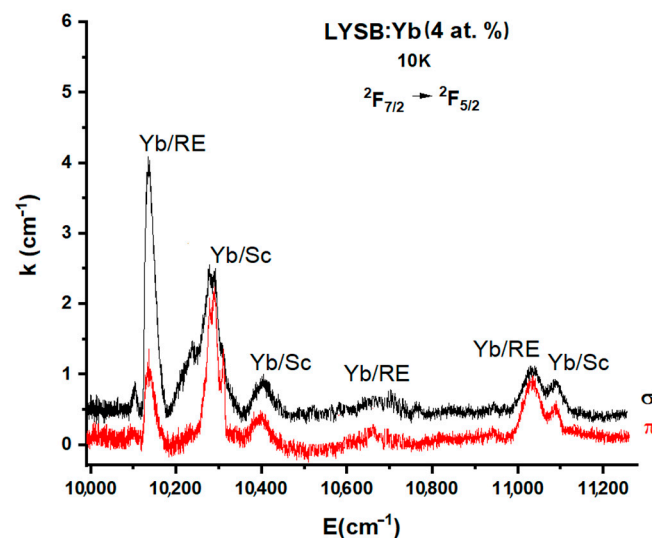
The polarized absorption cross-section spectra of  $\text{Yb}^{3+}$  ions assigned to the  ${}^2\text{F}_{7/2} \rightarrow {}^2\text{F}_{5/2}$  transitions at room temperature are presented in Figure 21. One can observe that the absorption cross-section ( $\sigma_{\text{abs}}$ ) corresponding to the line centered at 904 nm was higher for  $\pi$ -polarization, having a maximum value of  $\sigma_{\text{abs}} = 0.37 \times 10^{-20} \text{ cm}^2$ . On the other hand, the absorption cross-section at 980 nm was higher for  $\sigma$ -polarization, having a maximum value of  $\sigma_{\text{abs}} = 0.6 \times 10^{-20} \text{ cm}^2$  with an associated FWHM of 33 nm. Compared to other huntite-type crystals, the value of  $\sigma_{\text{abs}}$  at 980 nm was smaller than that of the well-known

YAB:Yb crystal ( $\sigma_{\text{abs}} = 3.4 \times 10^{-20} \text{ cm}^2$ ) [45] and close to the value for the LGSB:Yb crystal ( $\sigma_{\text{abs}} = 0.47 \times 10^{-20} \text{ cm}^2$ ) [46]. However, the FWHM bandwidth was larger, with a factor of 1.65, than the corresponding value for the YAB:Yb crystal (FWHM of 20 nm at 975 nm) [45], thus being advantageous for laser diode pumping.



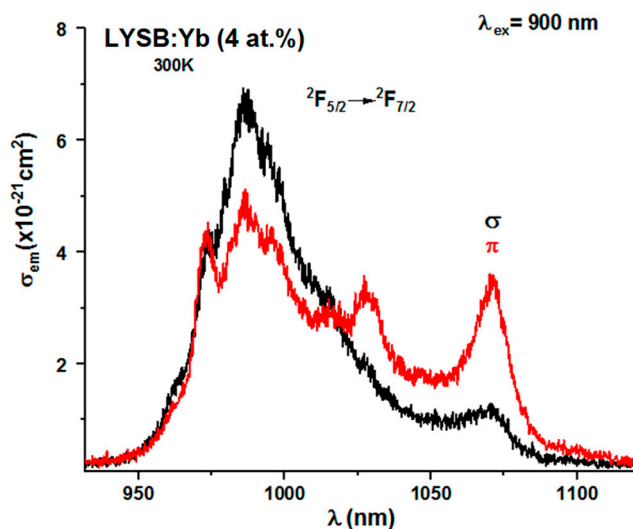
**Figure 21.** Polarized absorption cross-section spectra of LYSB:Yb (4 at.%) crystal at room temperature. Reprinted with permission from ref. [44], copyright 2020, Elsevier.

Figure 22 shows low-temperature (10 K) absorption spectra of the LYSB:Yb (4 at.%) crystal recorded in polarized light. The main absorption lines were broadened, and additional lines of weak intensity were observed in the vicinity of the electronic transitions, indicating the existence of different  $\text{Yb}^{3+}$  centers. The analysis of the  ${}^2\text{F}_{7/2} \rightarrow {}^2\text{F}_{5/2}$  transition at 10 K showed that  $\text{Yb}^{3+}$  ions substituted both RE (Yb/RE) and Sc ions (Yb/Sc) in the structure of LYSB:Yb (4 at.%) crystal, thus leading to the presence of two different  $\text{Yb}^{3+}$  centers [44].



**Figure 22.** Low-temperature (10 K) absorption spectra in polarized light of LYSB:Yb (4 at.%) crystal. Yb/RE and Yb/Sc denote the absorption lines of  $\text{Yb}^{3+}$  ions associated with  $\text{Yb}^{3+}$  in the position of  $\text{RE}^{3+}$  (RE = La, Y) or  $\text{Sc}^{3+}$ , respectively. Reprinted with permission from ref. [44], copyright 2020, Elsevier.

The room-temperature polarized emission spectra of 4 at.% Yb<sup>3+</sup> ions doped in the LYSB host matrix under excitation at 900 nm are presented in Figure 23. Using the Füchtbauer-Ladenburg equation [47], the emission cross-sections in both polarizations corresponding to the  $^2F_{5/2} \rightarrow ^2F_{7/2}$  transition were determined, and the obtained values are shown in Table 10.



**Figure 23.** Polarized emission cross-section spectra of LYSB:Yb (4 at.%) crystal at room temperature. Reprinted with permission from ref. [44], copyright 2020, Elsevier.

**Table 10.** Emission cross-sections of LYSB:Yb (4 at.%) crystal.

Polarization	986	$\lambda_{\text{emission}}$ (nm)	
		1026	1070
		$\sigma_{\text{em}} (\times 10^{-21} \text{ cm}^2)$	
$\pi$	5.12	3.56	3.6
$\sigma$	6.84	2.1	1.33

The low-temperature (10 K) emission spectra measured in polarized light under 902 nm (Yb/Sc center) and 906 nm (Yb/RE center) selective excitation are presented in Figure 24. The spectra show inhomogeneously broadened lines with an asymmetrical shape and a variation in the intensity of the emission lines with the excitation wavelength and polarization [44]. The energy Stark levels of the  $^2F_{7/2}$  and  $^2F_{5/2}$  manifolds, corresponding to each Yb<sup>3+</sup>/RE<sup>3+</sup> and Yb<sup>3+</sup>/Sc<sup>3+</sup> center, were determined. The obtained results are summarized and compared to those of the isostructural LGSB:Yb crystal in Table 11.

**Table 11.** Positions of the Stark levels of Yb<sup>3+</sup> centers in LYSB:Yb [44] and LGSB:Yb crystals [46]. Reprinted with permission from ref. [44], copyright 2020, Elsevier.

Crystal	Manifold	Yb <sup>3+</sup> /RE <sup>3+</sup>	Yb <sup>3+</sup> /Sc <sup>3+</sup>
LYSB:Yb	$^2F_{7/2}$	0, 385, 562, 757	0, 250, 547, 950
	$^2F_{5/2}$	10,135, 10,659, 11,033	10,285, 10,405, 11,085
LGSB:Yb	$^2F_{7/2}$	0, 394, 545.5, 768.7	0, 86.8, 552.3, 927
	$^2F_{5/2}$	10,144, 10,678.6, 11,044	10,297, 10,412.6, 11,103.4

The room-temperature emission kinetics of the  $^2F_{5/2}$  level of Yb<sup>3+</sup> ions was measured under excitation from the same OPO laser using a Tektronix 2024B oscilloscope for the detection. The decay curves were recorded by monitoring the emission line at 1070 nm under selective excitation at 902 and 906 nm and are shown in Figure 25. To measure an accurate value of the  $^2F_{5/2}$  level lifetime, unaffected by reabsorption processes, the 4 at.

% LYSB:Yb powder sample was 99% diluted with KBr. The decay curves were measured to be about 1230  $\mu\text{s}$  for the Yb/RE center ( $\lambda_{\text{ex}} = 906 \text{ nm}$ ) and 1350  $\mu\text{s}$  for the Yb/Sc center ( $\lambda_{\text{ex}} = 902 \text{ nm}$ ), being long enough to allow efficient energy storage on the emitting level. Compared to other well-known Yb-doped crystals, the values of the  ${}^2\text{F}_{5/2}$  level lifetime for each Yb center in 4 at. % LYSB:Yb crystal were considerably higher than the values of 951  $\mu\text{s}$  obtained for Yb:YAG crystal [48] and 680  $\mu\text{s}$  for YAB:Yb crystal [45], indicating that 4 at. % LYSB:Yb crystal has suitable properties for generation of high-energy laser pulses.

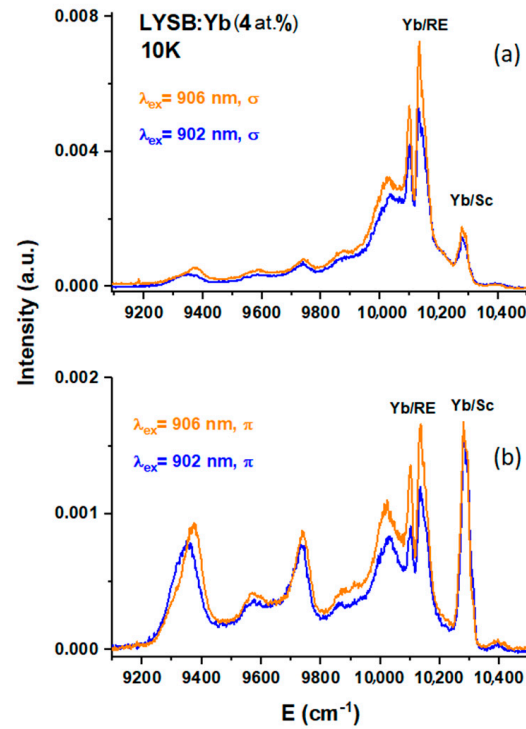


**Figure 24.** Emission spectra of LYSB:Yb (4 at.%) crystal under selective excitation in  $\sigma$ -polarization (a) and  $\pi$ -polarization (b) at 10 K. Adapted with permission from ref. [44], copyright 2020, Elsevier.

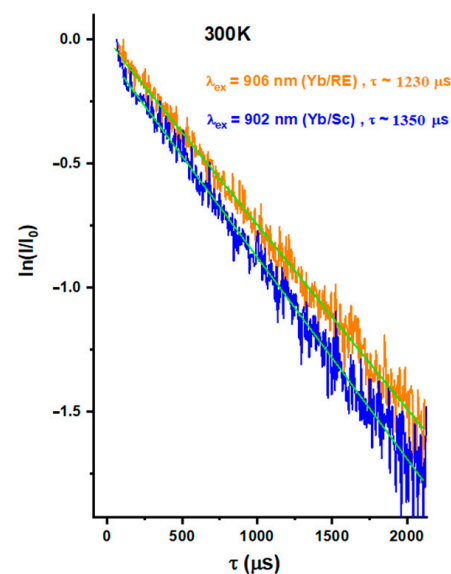


**Figure 25.** Luminescence decay curves of the  ${}^2\text{F}_{5/2}$  level in LYSB:Yb (4 at.%) crystal. Reprinted with permission from ref. [44], copyright 2020, Elsevier.

### 3.4. Laser Performances

A fiber-coupled (100  $\mu\text{m}$  diameter and  $\text{NA} = 0.22$ ) laser diode (LIMO Co) operating in quasi-continuous wave (quasi-CW) regime with emission centered at 971.5 nm having a repetition rate of 5 Hz and a pump pulse duration of 1 ms was employed for longitudinal pumping of the crystal sample. The uncoated *c*-cut 3.5 mm thick LYSB:Yb (4 at.%) crystal sample was placed inside an 8 mm long plane-plane resonator. The pumping mirror (PM) was highly transparent ( $T > 97\%$ ) in the wavelength range of 970–980 nm and highly reflective ( $R > 99.5\%$ ) in the 1020–1080 nm spectral domain. Out-coupling mirrors (OCM) with different transmissions ( $T = 1\%$ , 3%, and 5%) in the 1020–1080 nm wavelength domain were employed. Figure 26 shows the laser pulse energy ( $E_p$ ) as a function of the absorbed pump pulse energy ( $E_{\text{abs}}$ ). The LYSB:Yb (4 at.%) crystal sample delivered laser pulses with an energy of 1.23 mJ for an absorbed pump pulse energy of 4.52 mJ in the case of OCM with  $T = 3\%$ . The slope efficiency ( $\eta_{\text{sa}}$ ) was determined to be  $\eta_{\text{sa}} = 0.61$ . The maximum energy of the laser pulses was raised to 1.5 mJ in the case of the OCM with  $T = 1\%$ , and the slope efficiency was  $\eta_{\text{sa}} = 0.57$ . The laser emission wavelength was centered at  $\lambda_{\text{em}} = 1028.06$  nm with an FWHM of 0.85 nm. As seen in the inset of Figure 26, the transverse laser beam distribution was symmetric, being very close to a Gaussian shape.

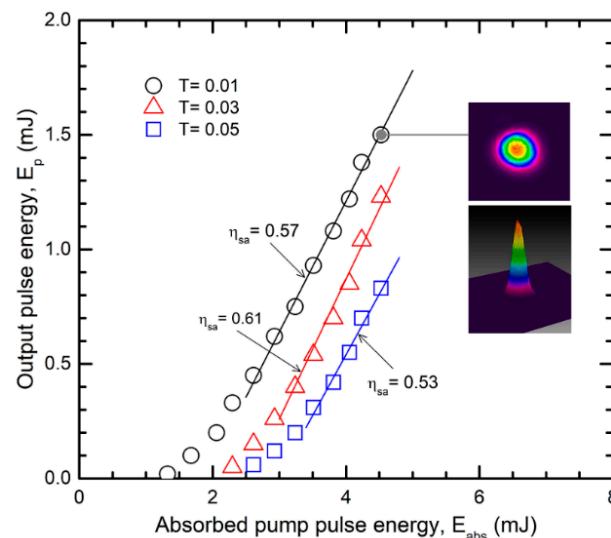


**Figure 26.** Laser pulse energy ( $E_p$ ) versus absorbed energy of the pump pulse ( $E_{\text{abs}}$ ). The laser beam distribution at the highest output level is shown in the figure inset. Reprinted with permission from ref. [44], copyright 2020, Elsevier.

Table 12 shows a comparison of laser emission performances of LYSB:Yb, LGSB:Yb, and YAB:Yb crystals operating in the quasi-CW regime. All of the presented active media were not antireflection-coated. In terms of slope efficiency, the value of  $\eta_{\text{sa}} = 0.61$  obtained for the LYSB:Yb (4 at.%) crystal is higher than the values obtained for LGSB:Yb ( $\eta_{\text{sa}} = 0.44$ ) [46] and YAB:Yb ( $\eta_{\text{sa}} = 0.58$ ) [49] crystals, proving the good intrinsic properties of the LYSB:Yb (4 at.%) crystal to generate laser emissions in the 1  $\mu\text{m}$  range with high efficiency.

**Table 12.** Laser emission characteristics in quasi-CW operation of uncoated LYSB:Yb, LGSB:Yb, [44,46], and YAB:Yb [49] crystals.

Crystal	Yb <sup>3+</sup> Ions Doping Concentration (at.%)	$\lambda_{\text{pump}}$ (nm)	$\lambda_{\text{emission}}$ (nm)	T (OCM Transmission)	$\eta_{\text{sa}}$
LYSB:Yb	4	971.5	1028.06	0.03	0.61
LGSB:Yb	12.9	972	1069.4	0.03	0.44
YAB:Yb	10	970	1043	0.029	0.58

#### 4. Conclusions

This review presents the development of Czochralski-grown LYSB and LYSB:Yb crystals. Taking into account the incongruent melting of these compounds, the initial melt compositions were refined; a particular thermal setup was engineered, and the rotation and pulling speeds were optimized at 810 rpm and 2 mm/h, respectively, to obtain high-quality crystals. The chemical composition of the undoped LYSB grown crystal was determined to be  $\text{La}_{0.78}\text{Y}_{0.32}\text{Sc}_{2.90}(\text{BO}_3)_4$ . Optical measurements revealed a large transparency window in the wavelength range of 2,002,800 nm. Moreover, the LYSB crystal had a high laser-induced damage threshold of  $20 \text{ J/cm}^2$  ( $\tau_p = 10 \text{ ns}$ ,  $\lambda = 1064 \text{ nm}$ ). The NLO characterization revealed that it is type-I and -II phase-matchable over a broad range of fundamental wavelengths, and the SHG phase-matching lower limit was found to correspond to the fundamental wavelength of 579 nm. The effective nonlinear coefficient ( $d_{\text{eff}}$ ) was determined to be  $1.13 \text{ pm/V}$ . Considering all of these favorable properties, it can be assumed that Czochralski-grown LYSB-type crystals constitute a new class of highly efficient NLO crystals for second-order applications, especially SHG of high-power or high-energy laser beams.

The LYSB:Yb crystal composition was determined as being  $\text{La}_{0.78}\text{Y}_{0.32}\text{Yb}_{0.04}\text{Sc}_{2.86}(\text{BO}_3)_4$ . The effective segregation coefficient ( $k_{\text{eff}}$ ) of  $\text{Yb}^{3+}$  ions in the LYSB crystal was determined to be  $k_{\text{eff}} = 0.8$ . The transmission spectrum showed that the cut-off wavelength was red-shifted by 20 nm compared to the undoped crystal, having a value of 220 nm. This shift can be attributed to  $\text{Yb}^{3+}$  insertion in both  $\text{RE}^{3+}$  ( $\text{RE} = \text{La}, \text{Y}$ ) and  $\text{Sc}^{3+}$  ion sites, leading to a modification of the contents of RE and Sc cations in the LYSB host crystal. The spectroscopic investigations revealed an intrinsic disorder in the structure of LYSB:Yb (4 at.%) crystal, thus offering inhomogeneously broadened absorption and emission bands. The LYSB:Yb (4 at.%) crystal delivered laser pulses with 1.23 mJ of energy for an absorbed pump pulse energy of 4.52 mJ with a high slope efficiency of  $\eta_{\text{sa}} = 0.61$ . The laser emission wavelength was centered at  $\lambda_{\text{em}} = 1028.06 \text{ nm}$ . The efficient laser emission at  $\sim 1028 \text{ nm}$  together with the good NLO properties to generate radiation at  $\sim 514 \text{ nm}$  via SHG make the LYSB:Yb (4 at.%) crystal a very promising medium to be used in self-frequency doubling configuration. Based on the successful growth by the Czochralski method of high-quality LYSB and LYSB:Yb (4 at.%) crystals, it can be stated that these types of crystals are very attractive candidates for various NLO and/or laser applications.

**Author Contributions:** Conceptualization, A.B. and L.G.; writing—original draft preparation, A.B., M.G. and C.G.; formal analysis, C.G. and L.G.; investigation, A.B., M.G., C.G., F.V. and L.G.; data curation, A.B., M.G., C.G., F.V. and L.G.; writing—review and editing, A.B. and L.G.; supervision, L.G. All authors have read and agreed to the published version of the manuscript.

**Funding:** This work was financed by the Romanian Ministry of Research, Innovation and Digitization through grant agreement PCE 49/2021, project number PN-III-P4-ID-PCE-2020-2203.

**Data Availability Statement:** Not applicable.

**Acknowledgments:** The authors thank George Stanciu, Stefania Hau, Gabriela Croitoru, and Nicolaie Pavel (INFLPR, Laboratory of Solid-State Quantum Electronics, 077125 Magurele, Romania) for their support in crystal characterization.

**Conflicts of Interest:** The authors declare no conflict of interest.

#### References

1. Mills, A.D. Crystallographic Data for New Rare Earth Borate Compounds,  $\text{RX}_3(\text{BO}_3)_4$ . *Inorg. Chem.* **1962**, *1*, 960–961. [[CrossRef](#)]
2. Chen, C.; Wu, Y.; Li, R. The Anionic Group-Theory of the Non-Linear Optical Effect and its Applications in the Development of New High-Quality NLO Crystals in the Borate Series. *Int. Rev. Phys. Chem.* **1989**, *8*, 65–91. [[CrossRef](#)]
3. Leonyuk, N.I.; Leonyuk, L.I. Growth and characterization of  $\text{RM}_3(\text{BO}_3)_4$  crystals. *Prog. Cryst. Growth Charact.* **1995**, *31*, 179–278. [[CrossRef](#)]
4. Tran, T.T.; Yu, H.; Rondinelli, J.M.; Poeppelmeier, K.R.; Halasyamani, P.S. Deep ultraviolet nonlinear optical materials. *Chem. Mater.* **2016**, *28*, 5238–5258. [[CrossRef](#)]

5. Durmanov, S.T.; Kuzmin, O.V.; Kuzmicheva, G.M.; Kutovoi, S.A.; Martynov, A.A.; Nesynov, E.K.; Panyutin, V.L.; Rudnitsky, Y.P.; Smirnov, G.V.; Hait, V.L.; et al. Binary rare-earth scandium borates for diode-pumped lasers. *Opt. Mater.* **2001**, *18*, 243–284. [[CrossRef](#)]
6. Li, Y.; Aka, G.; Kahn-Harari, A.; Vivien, D. Phase transition, growth, and optical properties of  $\text{Nd}_x\text{La}_{1-x}\text{Sc}_3(\text{BO}_3)_4$  crystals. *J. Mater. Res.* **2001**, *16*, 38–44. [[CrossRef](#)]
7. Ye, N.; Stone-Sundberg, J.; Hruschka, M.; Aka, G.; Kong, W.; Keszler, D. Nonlinear optical crystal  $\text{Y}_x\text{La}_y\text{Sc}_z(\text{BO}_3)_4$  ( $x + y + z = 4$ ). *Chem. Mater.* **2005**, *17*, 2687–2692. [[CrossRef](#)]
8. Ye, N.; Zhang, Y.; Chen, W.; Keszler, D.; Aka, G. Growth of nonlinear optical crystal  $\text{Y}_{0.57}\text{La}_{0.72}\text{Sc}_{2.71}(\text{BO}_3)_4$ . *J. Cryst. Growth* **2006**, *292*, 464–467. [[CrossRef](#)]
9. Li, W.; Huang, L.; Zhang, G.; Ye, N. Growth and characterization of nonlinear optical crystal  $\text{Lu}_{0.66}\text{La}_{0.95}\text{Sc}_{2.39}(\text{BO}_3)_4$ . *J. Cryst. Growth* **2007**, *307*, 405–409. [[CrossRef](#)]
10. Xu, X.; Ye, N.  $\text{Gd}_x\text{La}_{1-x}\text{Sc}_3(\text{BO}_3)_4$ : A new nonlinear optical crystal. *J. Cryst. Growth* **2011**, *324*, 304–308. [[CrossRef](#)]
11. Xu, X.; Wang, S.; Ye, N. A new nonlinear optical crystal  $\text{Bi}_x\text{La}_y\text{Sc}_z(\text{BO}_3)_4$  ( $x + y + z = 4$ ). *J. Alloys Compd.* **2009**, *481*, 664–667. [[CrossRef](#)]
12. Gheorghe, L.; Khaled, F.; Achim, A.; Voicu, F.; Loiseau, P.; Aka, G. Czochralski Growth and Characterization of Incongruent Melting  $\text{La}_x\text{Gd}_y\text{Sc}_z(\text{BO}_3)_4$  ( $x + y + z = 4$ ) Nonlinear Optical Crystal. *Cryst. Growth Des.* **2016**, *16*, 3473–3479. [[CrossRef](#)]
13. Gheorghe, L.; Greculeasa, M.; Broasca, A.; Voicu, F.; Stanciu, G.; Belikov, K.N.; Bryleva, E.Y.; Gaiduk, O. Incongruent Melting  $\text{La}_x\text{Y}_y\text{Sc}_{4-x-y}(\text{BO}_3)_4$ : LYSB Nonlinear Optical Crystal Grown by the Czochralski Method. *ACS Appl. Mater. Interfaces* **2019**, *11*, 20987–20994. [[CrossRef](#)]
14. Shannon, R. Revised Effective Ionic-Radii and Systematic Studies of Interatomic Distances in Halides and Chalcogenides. *Acta Crystallogr. Sect. A* **1976**, *32*, 751–767. [[CrossRef](#)]
15. Maillard, A.A.; Maillard, R.S.; Loiseau, P.; Aka, G.; Villeval, P.; Rytz, D. Defect Similitude in LYSB and YAB Crystals and ONL Characterization. In Proceedings of the 2014 Advanced Solid State Lasers, OSA Technical Digest, Shanghai China, 16–21 November 2014. paper Ath2A.12.
16. Reshak, A.H.; Auluck, S.; Majchrowski, A.; Kityk, I.V. Optical second harmonic generation in Yttrium Aluminum Borate single crystals (theoretical simulation and experiment). *PMC Phys. B* **2008**, *1*, 8. [[CrossRef](#)]
17. Jaque, D.; Ramirez, M.O.; Bausa, L.E.; Sole, J.G.; Cavalli, E.; Spheghini, A.; Betinelli, M.  $\text{Nd}^{3+} \rightarrow \text{Yb}^{3+}$  energy transfer in the  $\text{YAl}_3(\text{BO}_3)_4$  nonlinear laser crystal. *Phys. Rev. B* **2003**, *68*, 035118. [[CrossRef](#)]
18. Broasca, A.; Greculeasa, M.; Voicu, F.; Stanciu, G.; Hau, S.; Gheorghe, C.; Gheorghe, L. Pr:LYSB as a new nonlinear optical crystal: Czochralski growth and optical characterization. *J. Alloys Compd.* **2022**, *908*, 164633. [[CrossRef](#)]
19. Born, M.; Wolf, E. *Principles of Optics*; Pergamon Press: Oxford, UK, 1975.
20. Boyd, G.D.; Ashkin, A.; Dziedzic, J.M.; Kleinman, D.A. Second-Harmonic Generation of Light with Double Refraction. *Phys. Rev.* **1965**, *137*, A1305–A1320. [[CrossRef](#)]
21. Taylor, D. Spectral Acceptance for Second-Harmonic Generation in  $\text{CD}^*\text{A}$ . *J. Appl. Phys.* **1975**, *46*, 3988–3991. [[CrossRef](#)]
22. Hagen, W.F.; Magnante, P.C. Efficient Second-Harmonic Generation with Diffraction-Limited and High-Spectral-Radiance Nd-Glass Lasers. *J. Appl. Phys.* **1969**, *40*, 219–224. [[CrossRef](#)]
23. Lin, Z.S.; Lin, J.; Wang, Z.Z.; Wu, Y.C.; Ye, N.; Chen, C.T.; Li, R.K. Theoretical calculations and predictions of the nonlinear optical coefficients of borate crystals. *J. Phys. Condens. Matter* **2001**, *13*, R369. [[CrossRef](#)]
24. Liu, H.; Chen, X.; Huang, L.X.; Xu, X.; Zhang, G.; Ye, N. Growth and optical properties of UV transparent YAB crystals. *Mater. Res. Innov.* **2011**, *15*, 140–144. [[CrossRef](#)]
25. Yu, X.; Yue, Y.; Yao, J.; Hu, Z.G.  $\text{YAl}_3(\text{BO}_3)_4$ : Crystal growth and characterization. *J. Cryst. Growth* **2010**, *312*, 3029–3033. [[CrossRef](#)]
26. Gapontsev, V.P.; Tyrtshynny, V.A.; Vershinin, O.I.; Davydov, B.L.; Oulianov, D.A. Third harmonic frequency generation by Type-I critically phase-matched  $\text{LiB}_3\text{O}_5$  crystal by means of optically active quartz crystal. *Opt. Express* **2013**, *21*, 3715–3720. [[CrossRef](#)]
27. Chen, C.; Wu, Y.; Li, R. The development of new NLO crystals in the borate series. *J. Cryst. Growth* **1990**, *99*, 790–798. [[CrossRef](#)]
28. Maillard, R.S.; Maillard, A.; Polgár, K. Visible and UV effective non-linear optical coefficients of  $\beta\text{-BaB}_2\text{O}_4$  as function of the growth technique. *Opt. Mater.* **2009**, *31*, 899–901. [[CrossRef](#)]
29. Kwon, T.Y.; Ju, J.J.; Cha, J.W.; Kim, J.N.; Yun, S.I. Characteristics of critically phase-matched second-harmonic generation of a  $\text{Li}_2\text{B}_4\text{O}_7$  crystal grown by the Czochralski method. *Mater. Lett.* **1994**, *20*, 211–215. [[CrossRef](#)]
30. Komatsu, R.; Sugawara, T.; Sassa, K. Growth and ultraviolet application of  $\text{Li}_2\text{B}_4\text{O}_7$  crystals: Generation of the fourth and fifth harmonics of  $\text{Nd}:\text{Y}_3\text{Al}_5\text{O}_{12}$  lasers. *Appl. Phys. Lett.* **1997**, *70*, 3492–3494. [[CrossRef](#)]
31. Sifi, A.; Klein, R.S.; Maillard, A.; Kugel, G.E.; Péter, A.; Polgár, K. Absolute non-linear optical coefficients measurements of  $\text{CsLiB}_6\text{O}_{10}$  single crystals by second harmonic generation. *Opt. Mater.* **2003**, *24*, 431–435. [[CrossRef](#)]
32. Mori, Y.; Kuroda, I.; Nakajima, S.; Sasaki, T.; Nakai, S. New nonlinear optical crystal: Cesium lithium borate. *Appl. Phys. Lett.* **1995**, *67*, 1818–1820. [[CrossRef](#)]
33. Sasaki, T.; Mori, Y.; Yoshimura, M. Progress in the growth of a  $\text{CsLiB}_6\text{O}_{10}$  crystal and its application to ultraviolet light generation. *Opt. Mater.* **2003**, *23*, 343–351. [[CrossRef](#)]
34. Liu, W.; Shen, H.Y.; Zhang, G.F.; Zhang, D.Y.; Zhang, G.; Lin, W.X.; Zeng, R.R.; Huang, C.H. Studies on the phase-matching condition and the cut-off wavelength of Nb:  $\text{KTiOPO}_4$  crystal. *Opt. Commun.* **2000**, *185*, 191–196. [[CrossRef](#)]

35. Moorthy, S.G.; Kumar, F.J.; Balakumar, S.; Subramanian, C.; Ramasamy, P. Top seeded solution growth of  $\text{KTiOPO}_4$  (KTP) single crystals and their characterisation. *Mater. Sci. Eng. B* **1999**, *60*, 88–94. [[CrossRef](#)]
36. Yankov, P.; Schumov, D.; Nenov, A.; Monev, A. Laser damage tests of large flux-grown  $\text{KTiOPO}_4$  crystals. *Opt. Lett.* **1993**, *18*, 1771–1773. [[CrossRef](#)] [[PubMed](#)]
37. Phan, V.T.; Do, T.T.P.; Ho, T.M.; Nguyen, D.T.; Le, B.V.; Le, A.T.Q.; Duong, P.A.; Huynh, D.T. Fabrication of KDP crystal prisms for second harmonic generation. *Optik* **2018**, *171*, 230–236. [[CrossRef](#)]
38. Fujioka, K.; Matsuo, S.; Kanabe, T.; Fujita, H.; Nakatsuka, M. Optical properties of rapidly grown KDP crystal improved by thermal conditioning. *J. Cryst. Growth* **1997**, *181*, 265–271. [[CrossRef](#)]
39. Yu, Y.; Yu, Z.; Wang, L.; Sun, X. Ultralow-Loss Etchless Lithium Niobate Integrated Photonics at Near-Visible Wavelengths. *Adv. Optical Mater.* **2021**, *9*, 2100060. [[CrossRef](#)]
40. Furukawa, Y.; Yokotani, A.; Sasaki, T.; Yoshida, H.; Yoshida, K.; Nitanda, F.; Sato, M. Investigation of bulk laser damage threshold of lithium niobate single crystals by Q-switched pulse laser. *J. Appl. Phys.* **1991**, *69*, 3372–3374. [[CrossRef](#)]
41. Biaggio, I.; Looser, H.; Gunter, P. Intracavity frequency doubling of a diode pumped nd: Yag laser using a knbo3 crystal. *Ferroelectrics* **1989**, *94*, 157–161. [[CrossRef](#)]
42. Cussat-Blanc, S.; Ivanov, A.; Lupinski, D.; Freysz, E.  $\text{KTiOPO}_4$ ,  $\text{KTiOAsO}_4$ , and  $\text{KNbO}_3$  crystals for mid-infrared femtosecond optical parametric amplifiers: Analysis and comparison. *Appl. Phys. B* **2000**, *70*, S247–S252. [[CrossRef](#)]
43. Vijayan, N.; Bhagavannarayana, G.; Ramesh Babu, R.; Gopalakrishnan, R.; Maurya, K.K.; Ramasamy, P. A Comparative Study on Solution- and Bridgman-Grown Single Crystals of Benzimidazole by High-Resolution X-ray Diffractometry, Fourier Transform Infrared, Microhardness, Laser Damage Threshold, and Second-Harmonic Generation Measurements. *Cryst. Growth Des.* **2006**, *6*, 1542–1546. [[CrossRef](#)]
44. Broasca, A.; Greculeasa, M.; Voicu, F.; Hau, S.; Croitoru, G.; Gheorghe, C.; Pavel, N.; Gheorghe, L. Efficient near-infrared laser emission and nonlinear optical properties of a newly developed LYSB:Yb laser crystal. *J. Alloys Compd.* **2020**, *844*, 156143. [[CrossRef](#)]
45. Wang, P.; Dawes, J.M.; Dekker, P.; Knowles, D.S.; Piper, J.A.; Lu, B. Growth and evaluation of ytterbium-doped yttrium aluminum borate as a potential self-doubling laser crystal. *J. Opt. Soc. Am. B* **1999**, *16*, 63–69. [[CrossRef](#)]
46. Khaled, F.; Loiseau, P.; Voicu, F.; Achim, A.; Hau, S.; Gheorghe, C.; Croitoru, G.; Pavel, N.; Gheorghe, L.; Aka, G. Spectroscopic properties and laser performances of LGSB:Yb nonlinear optical crystal. *J. Alloys Compd.* **2016**, *688*, 510–517. [[CrossRef](#)]
47. Krupke, W.F. Induced-emission cross sections in neodymium laser glasses. *IEEE J. Quant. Electron.* **1974**, *10*, 450–457. [[CrossRef](#)]
48. Brenier, A.; Boulon, G. New criteria to choose the best  $\text{Yb}^{3+}$ -doped laser crystals. *Europhys. Lett.* **2001**, *55*, 647–652. [[CrossRef](#)]
49. Chen, Y.J.; Ye, N.; Lin, Y.F.; Luo, Z.D.; Huang, Y.D. Enhanced performances of  $\text{Yb}^{3+}:\text{YAl}_3(\text{BO}_3)_4$  laser crystal grown in  $\text{Li}_2\text{WO}_4$ - $\text{B}_2\text{O}_3$  flux. *Appl. Phys. B* **2011**, *104*, 145–149. [[CrossRef](#)]

**Disclaimer/Publisher’s Note:** The statements, opinions and data contained in all publications are solely those of the individual author(s) and contributor(s) and not of MDPI and/or the editor(s). MDPI and/or the editor(s) disclaim responsibility for any injury to people or property resulting from any ideas, methods, instructions or products referred to in the content.